รายงานวิจัยฉบับสมบูรณ์

โครงการ การประยุกต์ใช้แสงซินโครตรอนในการศึกษาสมบัติพิเศษของวัสดุขั้นสูงสำหรับใช้ในเครื่องอิเล็กทรอนิกส์ยุคใหม่

โดย ผศ. ดร. วรวัฒน์ มีวาสนา

เดือน ปี ที่เสร็จโครงการ

6/2558

สัญญาเลขที่ RSA5680052

รายงานวิจัยฉบับสมบูรณ์

โครงการ การประยุกต์ใช้แสงซินโครตรอนในการศึกษาสมบัติพิเศษของวัสดุขั้นสูงสำหรับใช้ในเครื่องอิเล็กทรอนิกส์ยุคใหม่

ผู้วิจัย ผศ. ดร. วรวัฒน์ มีวาสนา
สังกัด สาขาวิชาฟิสิกส์ สำนักวิชาวิทยาศาสตร์
มหาวิทยาลัยเทคโนโลยีสุรนารี

สนับสนุนโดยสำนักงานกองทุนสนับสนุนการวิจัย และ
มหาวิทยาลัยเทคโนโลยีสุรนารี

บทคัดย่อ

รหัสโครงการ : RSA5680052

ชื่อโครงการ : การประยุกต์ใช้แสงซินโครตรอนในการศึกษาสมบัติพิเศษของวัสดุขั้นสูงสำหรับใช้ในเครื่องอิเล็กทรอนิกส์ยุคใหม่

ชื่อนักวิจัย : ผศ. ดร. วรวัฒน์ มีวาสนา สังกัด สาขาวิชาฟิสิกส์ สำนักวิชาวิทยาศาสตร์ มหาวิทยาลัยเทคโนโลยีสุรนารี

E-mail Address : worawat@g.sut.ac.th

ระยะเวลาโครงการ : 2 ปี

ในโครงการนี้เพื่อเข้าใจถึงสมบัติที่แปลกใหม่ของวัสดุขั้นสูงสำหรับใช้ในเครื่องอิเล็กทรอนิกส์ยุคใหม่นั้น คณะวิจัยได้ใช้ประโยชน์จากเทคนิคแสงซินโครตรอนต่างๆ โดยเฉพาะเทคนิคโฟโตอิมิชชันสเปกโตรสโคปีในแบบแยกแยะเชิงมุม (ARPES) แบบแยกแยะสปิน (SR-PES) และ แบบแยกแยะธาตุ (XPS) มาทดลองวัดโครงสร้างอิเล็กทรอนิกส์จากสารในสองกลุ่มหลักๆ ได้แก่ 1. โลหะออกไซด์และโลหะแซลโคจิไนด์ 2. สารประกอบไดมอนดอยด์

ในส่วนแรกที่เกี่ยวกับโลหะออกไซด์และโลหะแซลโคจิไนด์คณะวิจัยสนใจเป็นพิเศษเกี่ยวกับโครงสร้างอิเล็กทรอนิกส์ของอิเล็กตรอนที่ถูกขังอยู่ในสองมิติ ซึ่งบ่อยครั้งพบว่าสมบัติบางอย่างที่ไม่มีในก้อนสารจะเกิดได้เมื่ออิเล็กตรอนที่ถูกขังอยู่ในสองมิตินี้ ในโครงการนี้คณะวิจัยได้ทำการวัดโครงสร้างอิเล็กทรอนิกส์ของโลหะแซลโคจิไนด์ 2 ชนิด ได้แก่ MoS_2 and WSe_2 และโลหะออกไซด์ 1 ชนิดได้แก่ $SrTiO_3$ สำหรับ MoS_2 นั้นคณะวิจัยพบวิธีใหม่ในการสร้างชั้นอะตอมอิสระโดยการแทรกธาตุโพแทสเซียมระหว่างชั้นอะตอมและสำหรับ WSe_2 คณะวิจัยสามารถเข้าใจในเชิงลึกถึงฟิสิกส์ของการโพลาไรซ์ของสปินในโครงสร้างอะตอมที่มีลักษณะสมมาตร สำหรับ $SrTiO_3$ คณะวิจัยได้เสนอแบบจำลองบนพื้นฐานของข้อมูลการทดลองและการคำนวณที่เกี่ยวกับแถบพลังงานที่แยกกันเพิ่มขึ้นซึ่งมีผลมาจากสมบัติของสปินที่แตกต่างกันในแต่ละวงโคจรของอิเล็กตรอนซึ่งอาจจะมีประโยชน์ในอุปกรณ์อิเล็กทรอนิกส์แบบสปิน ในส่วนที่ 2 ที่เกี่ยวกับ สารประกอบไดมอนดอยด์ คณะวิจัยเตรียมฟิล์มบางของไดมอนดอยด์ได้สำเร็จโดยใช้วิธีการตกเคลือบด้วยไอเคมี โดยคณะวิจัยพบว่าโครงสร้างอิเล็กทรอนิกส์ที่วัดได้แสดงถึงสมบัติการปลดปล่อยอิเล็กตรอนที่ดี และยังบ่งบอกถึงปริมาณของคาร์บอนในรูปแบบต่างๆ ได้อีกด้วย

คำหลัก : โลหะออกไซด์, โลหะแซลโคจิไนด์, $SrTiO_3$, MoS_2, WSe_2, ไดมอนดอยด์, โครงสร้างทางอิเล็กทรอนิกส์, เทคนิคโฟโตอิมิชชัน

Abstract

Project Code : RSA5680052

Project Title : Synchrotron-Radiation-Utilized Studies of Advanced Materials for Applications in New-Generation Electronics

Investigator : Asst. Prof. Dr. Worawat Meevasana, School of Physics, Institute of Science, Suranaree University of Technology

E-mail Address : worawat@g.sut.ac.th

Project Period: 2 years

In this project, to gain better understanding of novel electronic properties of potential materials for new-generation electronics, we utilize the synchrotron radiation techniques including angle-resolved photoemission spectroscopy (ARPES), x-ray photoemission spectroscopy (XPS) and spin-resolved spectroscopy (SR-PES) in studying the electronic structures of two groups of materials: 1) transition-metal oxides and chalcogenides and 2) carbon-based materials (mainly diamondoid).

Firstly, regarding the transition-metal oxides and chalcogenides, we focus on the electronic structures of electrons which are confined in two dimensions. In this confined state, novel properties, not available in bulk form, present themselves and sometimes can be useful for electronic applications. In this project, we measured the electronic structure of two metal-dichalcogenides (MoS_2 and WSe_2) and one metal oxide ($SrTiO_3$). For MoS_2, we find a new methodology in creating freestanding monolayer by potassium interaction and for WSe_2, we have a better understanding of the spin-polarized nature in a symmetric crystal. For $SrTiO_3$, based on experimental data and calculation, we propose a model about orbitally-enhanced spin-orbit splitting which may be useful for spintronic devices. Secondly, regarding the carbon-based materials (mainly diamondoid), we successfully prepare thin films of diamondoids using chemical-vapor-deposition method. From their measured electronic structure, we observe the electron emitting nature and are able to characterize the carbon-bonding types of the films.

Keywords : Transition-metal oxide, transition-metal dichalcogenide, $SrTiO_3$, MoS_2, WSe_2, diamondoid, electronic structure, photoemission spectroscopy

บทนำ

อุปกรณ์อิเล็กทรอนิกส์ในปัจจุบันส่วนใหญ่สร้างจากสารกึ่งตัวนำแบบดั้งเดิมโดยเฉพาะจากซิลิกอน สารกึ่งตัวนำตามชื่อนั้นคือมีสมบัติที่เปลี่ยนไปมาได้ระหว่างสภาพฉนวนไฟฟ้าและนำไฟฟ้าซึ่งนำมาพัฒนาเป็นทรานซิสเตอร์ที่ควบคุมการเปิดปิดของการนำไฟฟ้าและกลายเป็นเลข 0 และ 1 ในโลกดิจิตอล อย่างไรก็ตามการพัฒนาของชิปคอมพิวเตอร์ในปัจจุบันดูเหมือนว่าจะเข้ามาถึงจุดสิ้นสุดแล้วด้วยข้อจำกัดทางขนาดอะตอมที่ทำให้ความเร็วของการคำนวณไม่สามารถเพิ่มมากขึ้นอีกต่อไป ปัจจุบันเราจึงพยายามหาทางต่างๆเพื่อเอาชนะข้อจำกัดนี้ วิธีการแก้ปัญหานี้อาจต้องหาวัสดุใหม่ที่มีความสามารถสูงกว่าสารกึ่งตัวนำแบบดั้งเดิม ในโครงการนี้คณะวิจัยมีความสนใจวัสดุในสองกลุ่มได้แก่ 1) โลหะออกไซด์และโลหะแชลโคจิไนด์ และ 2) วัสดุคาร์บอน (โดยเฉพาะสารประกอบไดมอนดอยด์ (diamondoid))

ในกลุ่มแรกสำหรับสารโลหะออกไซด์และโลหะแชลโคจิไนด์นั้น คณะวิจัยสนใจในส่วนโครงสร้างอิเล็กทรอนิกส์ที่ในแบบสองมิติ สำหรับสารโลหะออกไซด์ความสนใจนั้นมาจากการค้นพบว่าสารประกอบสตรอนเทียมไททาเนต ($SrTiO_3$) ซึ่งมีค่าคงที่ไดอิเล็กตริก (Static dielectric constant) ที่สูงนั้นถ้าถูกมาสร้างผิวสัมผัสของสารนี้กับโลหะออกไซด์ $LaAlO_3$ จะเกิดชั้นอิเล็กตรอนสองมิติที่มีสมบัติเฉพาะตัวทางไฟฟ้าที่มีค่าความคล่องตัวของอิเล็กตรอน (Electron mobility) ที่สูงเหมาะแก่การมาใช้ออกแบบอุปกรณ์อิเล็กทรอนิกส์แบบใหม่ๆ ซึ่งชั้นอิเล็กตรอนสองมิตินี้นอกจากจะมีสมบัติของสารกึ่งนำไฟฟ้าแล้วยังมีสมบัติอื่นๆมากมาย เช่น การนำไฟฟ้ายิ่งยวดแบบสองมิติ สมบัติเชิงแม่เหล็ก และ มีค่าสัมประสิทธิ์เทอร์โมอิเล็กตริกที่สูง เป็นต้น ในลักษณะที่คล้ายกันสารโลหะแชลโคจิไนด์ (เช่น MoS_2 และ WSe_2) ก็มีโครงสร้างอิเล็กทรอนิกส์เชิงสองมิติโดยเฉพาะเมื่อสารมีความบางมากๆ นอกจากจะมีสมบัติของสารกึ่งนำไฟฟ้าและแสดงประสิทธิภาพที่สูงเมื่อนำมาใช้ในตัวทรานซิสเตอร์แล้ว สารโลหะแชลโคจิไนด์ยังมีสมบัติในเชิงแสงและฟิสิกส์ของสปินที่โดดเด่นซึ่งอาจจะนำมาใช้ออกแบบอุปกรณ์อิเล็กทรอนิกส์ที่มีความสามารถหลากหลายและแตกต่างจากที่มีในปัจจุบันได้

ในกลุ่มที่สองสำหรับวัสดุคาร์บอน ความน่าสนใจเริ่มมาจากงานวิจัยที่ออกมามากมายเกี่ยวกับสารกราฟีน (graphene) ซึ่งถูกค้นพบโดย Geim และ Novoselov ซึ่งได้รางวัลโนเบลสาขาฟิสิกส์ในปี ค.ศ. 2010 กราฟีนถูกก็ถูกค้นพบว่ามีสมบัติเชิงไฟฟ้าที่โดดเด่นมากมาย เช่น ค่าความคล่องตัวของอิเล็กตรอนที่สูงมหาศาล สภาพควอนตัมฮอลล์ที่อุณหภูมิห้อง เป็นต้น อย่างไรก็ตามงานวิจัยของกราฟีนก็มีออกมามากมายและมีการแข่งขันสูงในปัจจุบันเช่นกัน คณะวิจัยจึงเบนความสนใจและคิดว่าน่าจะยังมีสารประกอบคาร์บอนแบบอื่นๆ ที่น่าสนใจมากเช่นกันที่ยังคอยการค้นพบ คณะวิจัยจึงมาสนใจสารในกลุ่มที่เรียกว่า สารประกอบไดมอนดอยด์ (diamondoid) หรือ สารประกอบที่มีโครงสร้างอะตอมของคาร์บอนในระดับนาโน สารประกอบเหล่านี้น่าสนใจตรงที่น่าจะมีสมบัติต่างๆคล้ายกับเพชร แต่มีราคาที่ถูกมากเหมาะแก่การพัฒนามาใช้ในเชิงอุตสาหกรรม

ในโครงการนี้คณะวิจัยได้พยายามศึกษาสมบัติทางแม่เหล็กและไฟฟ้าของสารประกอบเหล่านี้จากข้อมูลที่เรียกว่าโครงสร้างอิเล็กทรอนิกซ์ซึ่งวัดได้โดยใช้เทคนิคแสงซินโครตรอน โดยเฉพาะเทคนิคโฟโตอิมิชชันสเปกโตรสโคปีในแบบแยกแยะเชิงมุม (ARPES) แบบแยกแยะสปิน (SR-PES) และ แบบแยกแยะธาตุ (XPS) โดยสารที่นำมาวัดได้แก่ $SrTiO_3$, MoS_2, WSe_2 และ ฟิล์มไดมอนดอยด์ ซึ่งมีรายละเอียดโครงสร้างอิเล็กทรอนิกซ์ที่น่าสนใจซึ่งถูกอธิบายเป็นส่วนๆในหัวข้อ “ผลการทดลอง”

วิธีทดลอง

ก. ขั้นตอนการเตรียมสารตัวอย่างโลหะออกไซด์และโลหะแซลโคจิไนด์

สำหรับผลึกสตรอนเทียมไททาเนตที่มีสารเจือของธาตุ La (แทนที่ธาตุ Sr) ที่มีความเข้มข้นต่ำเพื่อให้นำไฟฟ้าเพียงเล็กน้อยเพื่อสะดวกต่อการทดลองโฟโตอิมิชชัน ทดสอบโดยการวัดความต้านทาน ถ้าไม่ทราบระนาบของผลึกอาจจะต้องวัดระนาบของผลึกด้วยเครื่อง X-ray Diffraction แบบ Laue ในการทดลองโฟโตอิมิชชันต้องการความสะอาดสูงมาก วิธีหนึ่งที่ใช้ทั่วไปคือการทำให้ผลึกแตกออกในสุญญากาศเพื่อได้พื้นผิวที่สะอาด เพื่อที่ผลึกแตกออกอย่างราบเรียบ ก่อนนำผลึกไปวัดเทคนิคที่สำคัญคือการตัดผลึกบางส่วนในแนวที่ผลึกจะแตกออก การตัดนำร่องนี้ต้องอาศัยเครื่องตัดผลึกแบบเส้นลวด หลังจากการตัดนำร่องต้องล้างผลึกให้สะอาดด้วยแอลกอฮอล์ก่อนใส่เข้าสู่ระบบสุญญากาศในเครื่องโฟโตอิมิชชัน สำหรับโลหะแซลโคจิไนด์มีการเตรียมคล้ายกันแต่ไม่ต้องมีการตัดนำร่องเหมือนผลึกสตรอนเทียมไททาเนต

ข. ขั้นตอนการวัดโครงสร้างทางอิเล็กทรอนิกส์โดยเทคนิคโฟโตอิมิชชันแบบต่างๆ (ARPES, SR-PES และ XPS)

เทคนิคโฟโตอิมิชชันอาศัยหลักการเดียวกับปรากฏการณ์โฟโตอิเล็กทริก โดยแสงที่มีพลังงานสูงจะเข้าไปกระตุ้นอิเล็กตรอนที่อยู่ภายในให้หลุดออกมา โดยเครื่องจะทำการวัดจำนวนของอิเล็กตรอนที่หลุดออกมาที่พลังงานและมุมต่างๆ (ตามรูปที่ 1) เพื่อใช้ดูโครงสร้างอิเล็กทรอนิกส์ของวัสดุที่สนใจ สำหรับโครงการนี้จะเลือกอุณหภูมิสองช่วงคืออุณหภูมิห้อง และอุณหภูมิประมาณ 20 เคลวินโดยใช้ฮีเลียมเหลวในการควบคุมอุณหภูมิ หลังจากปรับอุณหภูมิให้เท่ากับอุณหภูมิที่จะศึกษาแล้วทำผลึกให้แตกออก สามารถตรวจสอบความเรียบได้โดยการฉายแสงเลเซอร์เพื่อดูภาพสะท้อน หลังจากนั้นทำการวัดโครงสร้างทางอิเล็กทรอนิกส์ โดยฉายแสงยูวีที่มีความเข้มสูงจากเครื่องซินโครตรอนที่พลังงานโฟตอนระหว่าง 40-80 eV สำหรับเทคนิค ARPES และ SR-PES แต่สำหรับเทคนิค XPS พลังงานแสงจะกำหนดโดยธาตุที่ต้องการศึกษา หมายเหตุ สำหรับสารประกอบ $SrTiO_3$ การฉายแสงดังกล่าวยังทำให้เกิดชั้นอิเล็กตรอนสองมิติขึ้นด้วยซึ่งอยู่รวมกับโครงสร้างอิเล็กตรอนในก้อนสาร จากนั้นวัดสเปกตรัมความหนาแน่นของโฟโตอิเล็กตรอนที่หลุดออกมาเป็นฟังก์ชันของพลังงาน เปลี่ยนไปวัดที่ค่ามุม

ต่าง ๆเพื่อเป็นการแยกแยะเชิงมุมเพื่อดูการกระจายตัวที่ค่าโมเมนตัมต่าง ๆซึ่งจะเป็นข้อมูลสำคัญในโครงการนี้

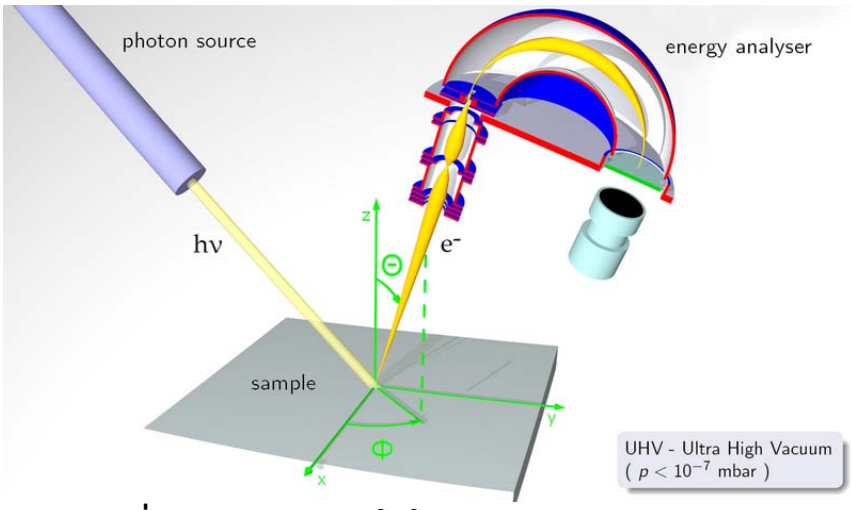

รูปที่ 1 แผนภาพเทคนิคโฟโตอิมิชชันแบบแยกแยะเชิงมุม

ค. ขั้นตอนการวัดต้านทานไฟฟ้าบนพื้นผิวหลังการฉายแสงยูวี

นำสารตัวอย่างเข้าสู่ระบบสุญญากาศซึ่งเป็นการเพิ่มประสิทธิภาพของการฉายแสง เนื่องจากแสงยูวีจะถูกดูดกลืนได้ง่ายในอากาศปกติทำให้ความเข้มลดลง หลังจากความดันอากาศอยู่ในช่วงต่ำกว่า 10^{-7} torr จะทำการตรวจสอบสภาพนำไฟฟ้าบนผิวโดยการวัดความต้านทานก่อนฉายแสง ต่อจากนั้นฉายแสงบนสารตัวอย่างด้วยแสงยูวีที่ปรับ ความเข้มแสง พลังงาน และขนาดของลำแสงให้มีค่าตามที่ต้องการ แล้วจึงตรวจสอบสภาพนำไฟฟ้าบนผิว โดยการวัดความต้านทานหลังฉายแสงอีกครั้ง หมายเหตุ เพื่อช่วยในการวัดความต้านทานของผลึกที่เป็นฉนวนการทำขั้วไฟฟ้าโดยเทคนิค sputtering อาจจำเป็น

ง. ขั้นตอนการเตรียมฟิล์มไดมอนดอยด์

มีการเตรียมฟิล์มไดมอนดอยด์ 2 แบบ แบบแรกทำได้โดยการปลูกฟิล์มไดมอนดอยด์ที่เรียกว่า Self assembly monolayer โดยการจุ่มแผ่นฟิล์มบางของทองนสารละลาย adamantane ซึ่งผสม toluene และ ethanol ประมาณครึ่ง ๆ แช่ไว้ประมาณ 24 ชม แล้วยกแผ่นฟิล์มบางของทองออกจะมีไดมอนดอยด์ติดอยู่บาง ๆ แบบที่ 2 ทำได้โดยวิธี Chemical Vapor Deposition (CVD) ซึ่งใช้แผ่นโลหะโดยให้อุณหภูมิสูงประมาณ 1000 องศาเซลเซียสแล้วใส่แก๊ซของ adamantine เข้าไปจะได้แผ่นฟิล์มบาง ๆของไดมอนดอยด์

จ. ขั้นตอนการวิเคราะห์ผลและการเปรียบเทียบผลที่ได้กับการคำนวณ

ใช้โปรแกรม Igor ของบริษัท Wavematrics ในการวิเคราะห์ผลการทดลองเพื่อดูโครงสร้างทางอิเล็กทรอนิกส์โดยเฉพาะการกระจายตัวของอิเล็กตรอนในฟังก์ชั่นของพลังงาน

และโมเมนตัม หรือ Electron band dispersion ในช่วงพลังงานใกล้กับชั้นพลังงานเฟอร์มิ (ประมาณ 0-300 meV) เปรียบเทียบกับโครงสร้างอิเล็กทรอนิกส์ที่ได้จากการคำนวณโดยวิธี Local Density Approximation ที่มีอยู่แล้ว หรือผลการคำนวณเพิ่มเติมจากนักวิจัยร่วม จากนั้นทำการเปรียบเทียบกับผลการทดลองจากเทคนิคอื่นเช่น ค่ามวลประสิทธิ (Effective mass) ของอิเล็กตรอนจากค่าความต้านทาน หรือจากสมบัติทางแสงเพื่อเป็นการยืนยัน หรือในกรณีที่ผลการทดลองไม่ตรงกับผลการคำนวณ ข้อมูลส่วนที่ต่างกันนี้อาจจะช่วยบ่งบอกถึงที่มาของการกำเนิดสมบัติโดดเด่นของสตรอนเทียมไททาเนตที่กล่าวมาข้างต้นได้ นอกจากนี้ยังส่วนของการคำนวณหาชั้นพลังงานตามแบบจำลอง Quantum well เพื่อดูการเกิดชั้นอิเล็กตรอนสองมิติ

ผลการทดลองและบทวิจารณ์

1. โครงสร้างอิเล็กทรอนิกส์ของชั้นอะตอมเดี่ยวของ MoS_2 บนก้อนสาร

ในผลงานวิจัยนี้ (ตามเอกสารแนบที่ 1 ในภาคผนวก) ข้าพเจ้าและลูกศิษย์ปริญญาเอก (Tanachat Eknapakul) ได้เป็นผู้แต่งหลักโดยมีส่วนในการวางแผน วัดโครงสร้างอิเล็กทรอนิกส์ของ MoS_2 ด้วยเทคนิคโฟโตอิมิชชัน วิเคราะห์และเขียนบทความ

สำหรับงานวิจัยนี้คณะวิจัยสนใจในสมบัติของโลหะแซลโคจิไนด์ต่างๆที่เปลี่ยนไปเมื่อเปลี่ยนสภาพจากก้อนสาร (bulk) มาเป็นชั้นอะตอมเดี่ยว (monolayer) หรือเปลี่ยนสภาพจาก 3 มิติ มาเป็น 2 มิติ นั่นเอง [1] หนึ่งในสมบัติที่ว่านั้นคือมีสภาพที่มีช่องว่างแถบพลังงานเปลี่ยนไปจากแบบไม่ตรง (indirect band gap) มาเป็นแบบตรง (direct band gap) ของ MoS_2 [2]เมื่อจำนวนชั้นอะตอมของผลึกลดลงจนถึงหนึ่งชั้นอะตอม ในงานนี้ทางคณะวิจัยได้แสดงถึงวิธีการสร้างโครงสร้างอิเล็กทรอนิกส์ของ MoS_2 ที่คล้ายกับของชั้นอะตอมเดี่ยวด้วยการแทรกอะตอมของธาตุโพแทสเซียมระหว่างชั้นอะตอมของ MoS_2 [3] ซึ่งแกะกันด้วยแรงวันเดอร์วาลส์ซึ่งจะทำให้มีการขยายออกระยะห่างของอะตอมในแนวตั้งฉาก (ตามรูปที่ 2)

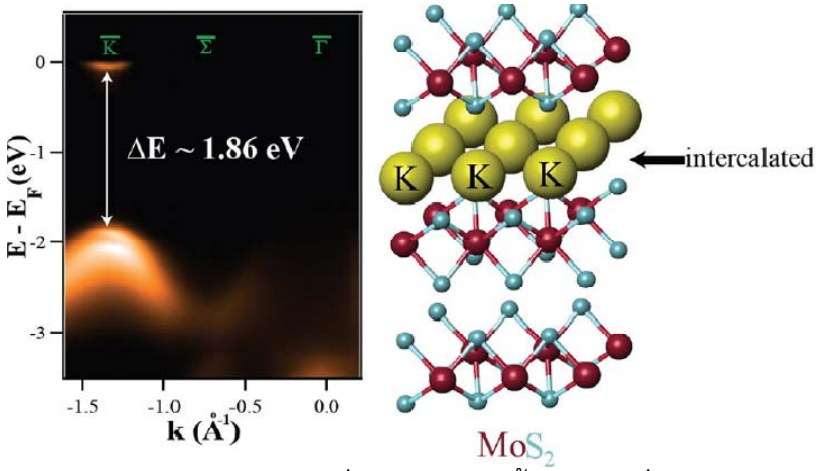

รูปที่ 2 โครงสร้างอิเล็กทรอนิกส์ของ MoS_2 ที่คล้ายกับของชั้นอะตอมเดี่ยว และแผนภาพการแทรกอะตอมของธาตุโพแทสเซียมระหว่างชั้นอะตอมของ MoS_2

จากผลการทดลองที่ได้จากเทคนิคโฟโตอิมิชชันสเปกโตรสโคปีแบบแยกแยะเชิงมุม (ARPES) ช่องว่างแถบพลังงานที่โมเมนตัมที่ตำแหน่ง **K** (ตามรูปที่ 2) มีค่าประมาณ 1.8 eV ซึ่งใกล้เคียงกับที่การทดลองอื่นได้จากการวัดช่องว่างแถบพลังงานของชั้นอะตอมเดี่ยว ทั้งนี้คณะวิจัยยังได้ทำการคำนวณแถบพลังงานจาก density functional theory (DFT) เมื่อมีการขยายของระยะอะตอมในแนวตั้งฉากจากการที่มีอะตอมของธาตุโพแทสเซียมเข้าไปแทรกอยู่ พบว่าแถบพลังงานมีลักษณะใกล้เคียงกับผลการทดลองเมื่ออัตราส่วนระหว่างระยะห่างแลตทิซในแนวตั้งฉากกับขนาน (c/a) มีค่าประมาณ 4.893 ตามรูปที่ 3 จากสิ่งที่ค้นพบนี้นอกจากช่วยยืนยันการศึกษาเชิงทฤษฎีแล้วยังเป็นแนวทางใหม่ที่ใช้ในการสร้างชั้นอะตอมเดี่ยวจากก้อนผลึกซึ่งอาจจะประยุกต์เชิงอุตสาหกรรมต่อไป

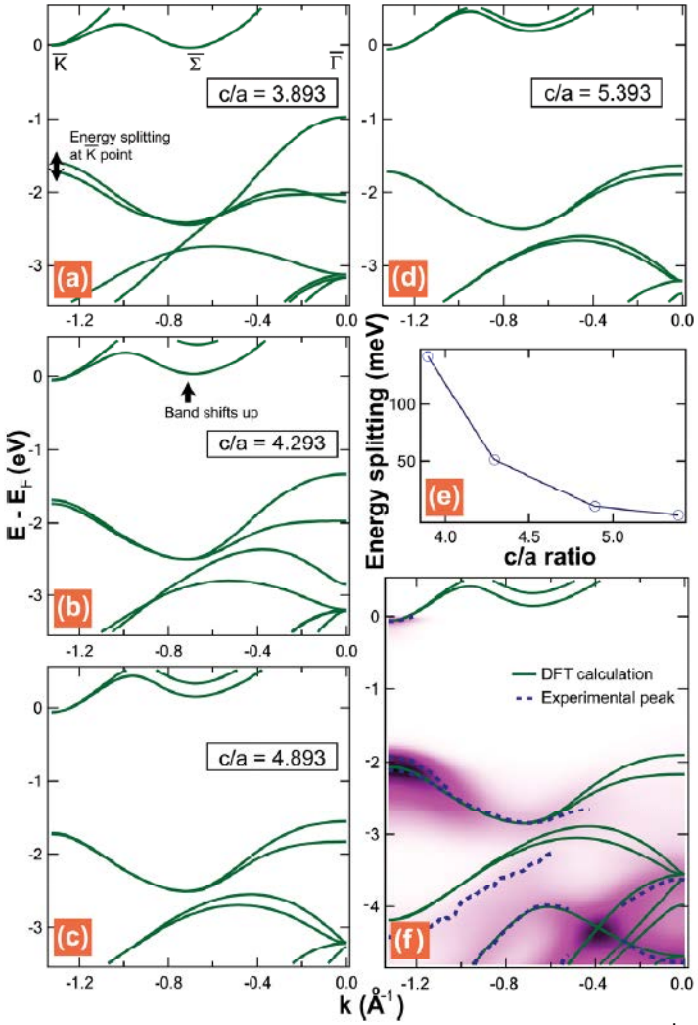

รูปที่ 3 การคำนวณแถบพลังงานจาก density functional theory (DFT) เมื่อมีการขยายของระยะอะตอมในแนวตั้งฉาก เพื่อใช้เทียบกับโครงสร้างอิเล็กทรอนิกส์ที่ได้จากการทดลอง

2. การสังเกตแถบพลังงานที่มีการโพลาไรซ์ของสปินในผลึกที่สมมาตรของ WSe_2

ในผลงานวิจัยนี้ (ตามเอกสารแนบที่ 2 ในภาคผนวก) ข้าพเจ้าและได้เป็นผู้แต่งร่วมโดยมีส่วนร่วมในการวัดโครงสร้างอิเล็กทรอนิกส์ของ WSe_2 ด้วยเทคนิคโฟโตอิมิชชัน

ในส่วนนี้เป็นการศึกษาโลหะแซลโคจิไนด์ที่ชื่อว่า WSe_2 โดยคณะวิจัยสนใจสมบัติทางแม่เหล็กและสถานะทางควอนตัมที่มีการโพลาไรซ์ของสปิน [4] และถ้าเรายิ่งสามารถควบคุมการสมบัติการโพลาไรซ์ของสปินได้ก็จะยิ่งมีประโยชน์ต่อการอุปกรณ์อิเล็กทรอนิกส์แบบใหม่ๆ ได้ อย่างไรก็ตามทฤษฎีโดยปกตินั้นการจะเกิดสมบัติทางสปินควรจะเกี่ยวข้อกับเสียสมมาตรของผลึก (Inversion symmetry breaking) ไปทางใดทางหนึ่ง แต่ที่น่าสนใจในที่นี้คือคณะวิจัยพบว่ามีการโพลาไรซ์ของสปินของแต่ละชั้นอะตอมในผลึกของ WSe_2 ซึ่งมีความสมมาตร [5] การศึกษานี้ใช้เทคนิคโฟโตอิมิชชันสเปกโตรสโคปีในแบบแยกแยะเชิงมุม (ARPES) (ตามรูปที่ 4) และแบบแยกแยะสปิน (SR-PES) (ตามรูปที่ 5)

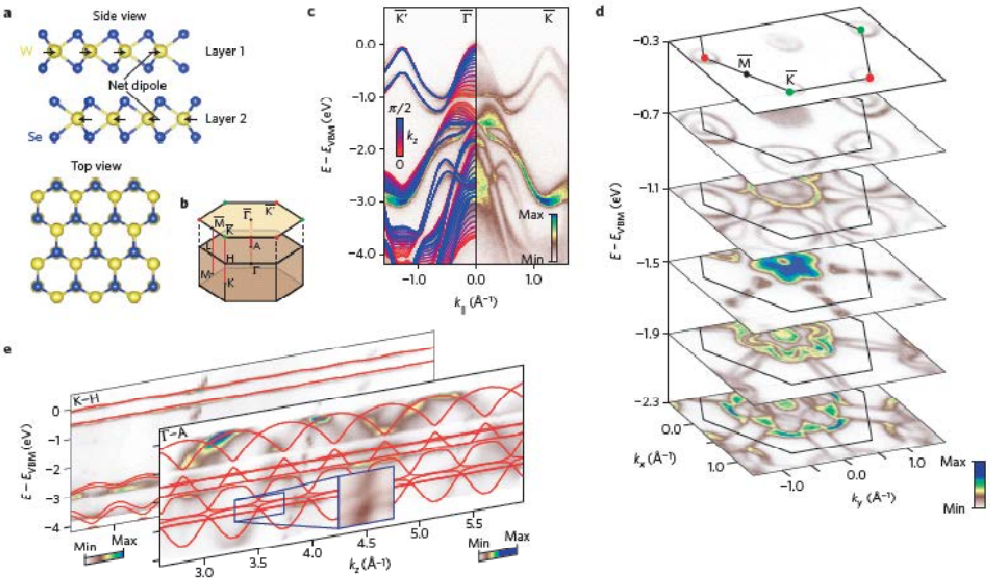

รูปที่ 4 โครงสร้างทางอะตอม (a) และโครงสร้างอิเล็กทรอนิกส์ของ WSe_2 ที่วัดด้วยเทคนิคโฟโตอิมิชชันสเปกโตรสโคปีแบบแยกแยะเชิงมุม (b-d)

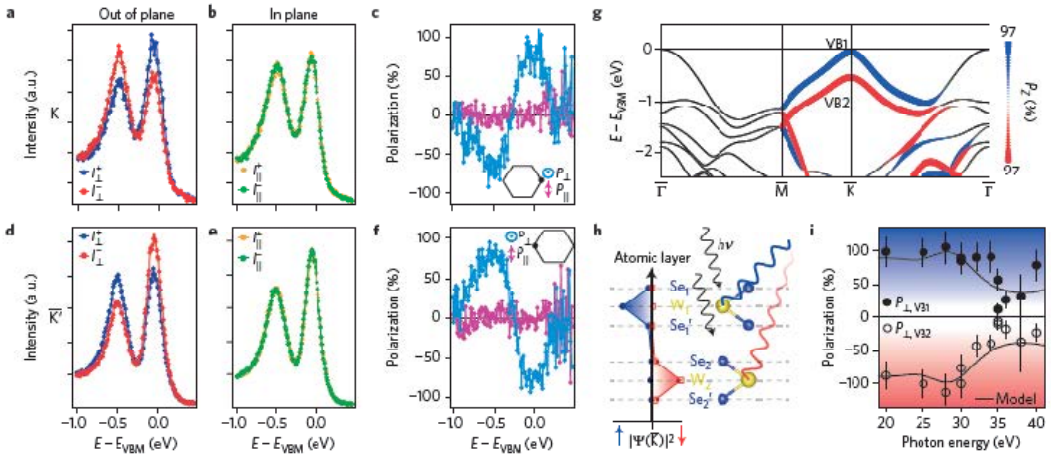

รูปที่ 5 โครงสร้างอิเล็กทรอนิกส์ของ WSe_2 ที่วัดด้วยเทคนิคโฟโตอิมิชชันสเปกโตรสโคปีแบบแยกแยะสปินซึ่งพบว่ามีการโพลาไรซ์ของสปินในแต่ละชั้นอะตอม

3. การศึกษาสมบัติทางสปินของอิเล็กตรอนในชั้นนำไฟฟ้าสองมิติบนผิวของผลึกสตรอนเทียมไททาเนต

ในผลงานวิจัยนี้ (ตามเอกสารแนบที่ 3 ในภาคผนวก) ข้าพเจ้าและลูกศิษย์ปริญญาเอก (Tanachat Eknapakul และ Pornpana Buaphet) ได้เป็นผู้แต่งร่วมโดยมีส่วนในการทดลองวัดโครงสร้างอิเล็กทรอนิกส์ของ $SrTiO_3$ ด้วยเทคนิคโฟโตอิมิชชัน

สำหรับงานวิจัยนี้คณะวิจัยสนใจในโครงสร้างอิเล็กทรอนิกส์ของชั้นอิเล็กตรอนสองมิติบนสารประกอบสตรอนเทียมไททาเนต ($SrTiO_3$) ตามรูปที่ 6 ซึ่งในผลงานที่ผ่านมาคณะวิจัยพบว่าชั้นอิเล็กตรอนสองมิตินี้เกิดขึ้นได้เมื่อมีการฉายแสงยูวีที่ได้จากแสงซินโครตรอน [6] และในงานวิจัยนี้ได้ทำการศึกษาต่อยอดเพื่อจะดูอันตรกิริยาระหว่างประจุ สปิน โมเมนตัมเชิงมุม และ อนุภาคโบซอน (เช่น โฟนอน เป็นต้น) โดยมีการคำนวณโครงสร้างอิเล็กทรอนิกส์จากแบบจำลอง tight binding รวมถึงการสร้างแบบจำลองการเกิดอันตรกิริยาระหว่างสปินกับโมเมนตัมเชิงมุม (spin-orbit interaction) ที่ไม่เหมือนกันในวงโคจรต่างๆของอิเล็กตรอน (orbital) ซึ่งส่งผลให้เกิดการแยกออกของแถบพลังงานซึ่งไม่เหมือนกับแบบดั้งเดิม (Rashba splitting) [7] ตามรูปที่ 7 โดยการแยกออกของแถบพลังงานนี้น่าจะส่งผลถึงสภาพแม่เหล็กของชั้นอิเล็กตรอนสองมิติบน $SrTiO_3$ ซึ่งอาจจะเป็นสมบัติหนึ่งซึ่งในไปใช้ออกแบบอุปกรณ์อิเล็กทรอนิกส์แบบใหม่ได้

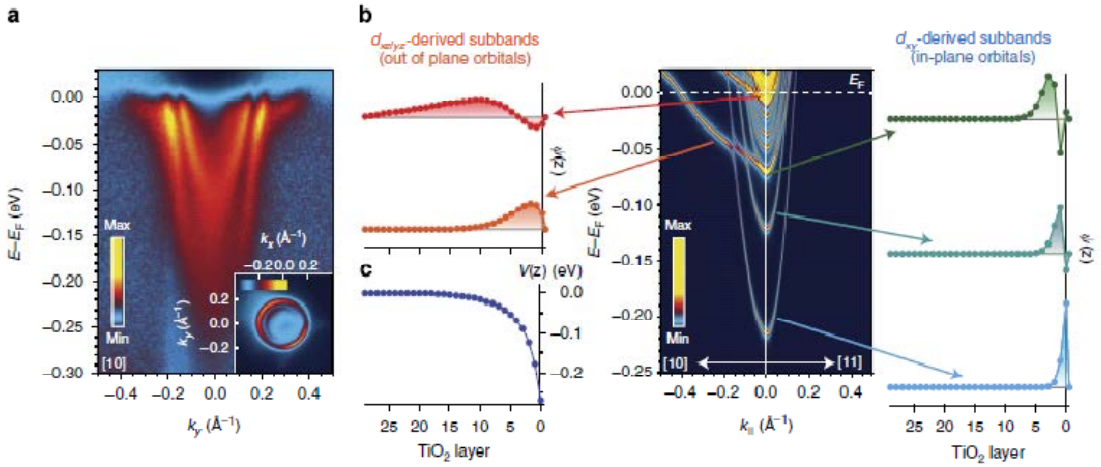

รูปที่ 6 โครงสร้างทางอิเล็กทรอนิกส์ของชั้นอิเล็กตรอนสองมิติบนผิวของ $SrTiO_3$ ที่ได้จากการทดลอง (ซ้าย) และ การคำนวณ (ขวา)

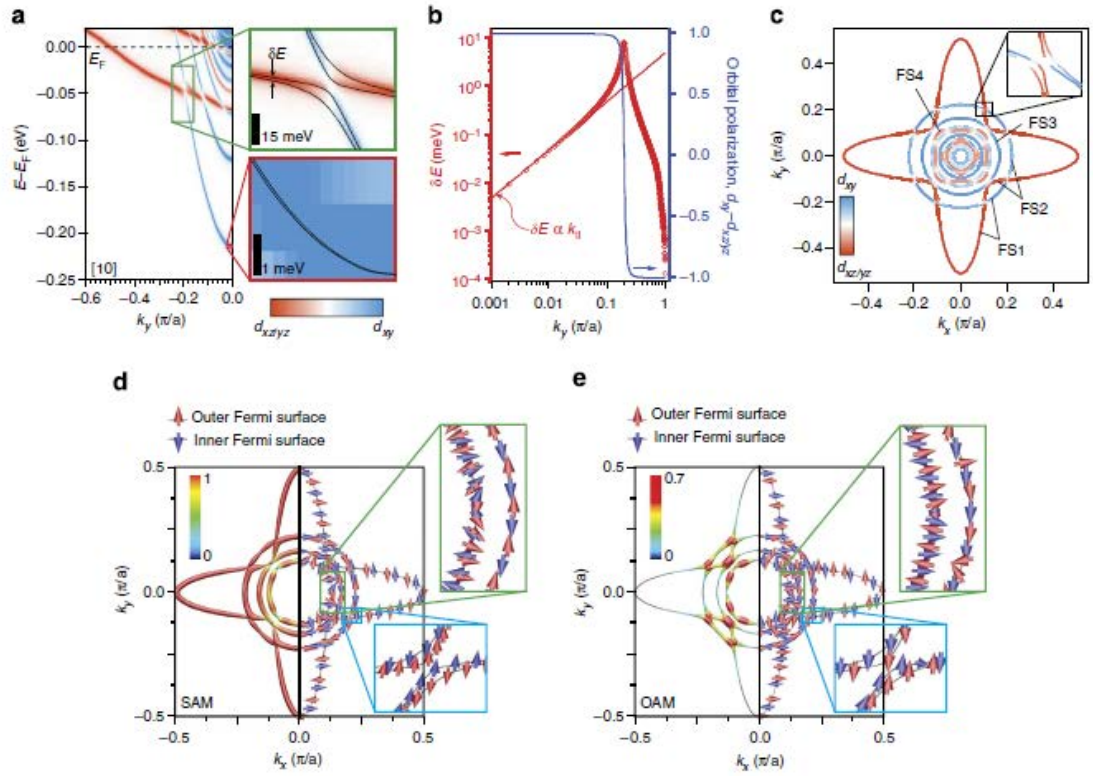

รูปที่ 7 การแยกออกของแถบพลังงานที่เกิดอันตรกิริยาระหว่างสปินกับโมเมนตัมเชิงมุมที่ไม่เท่ากันในวงโคจรของอิเล็กทรอนที่ต่างกัน

4. การสังเคราะห์ฟิล์มบางจากสารประกอบไดมอนดอยด์และสมบัติ

ในงานวิจัยส่วนนี้ยังเป็นงานวิจัยหลักของข้าพเจ้าและลูกศิษย์ปริญญาเอก (Sumeth Siriroj) มีผลทดลองที่น่าสนใจซึ่งนำมารายงานก่อนในเบื้องต้นดังด้านล่าง แต่ยังคงต้องศึกษาเพิ่มเติมและเขียนบทความเพื่อส่งตีพิมพ์ต่อไป ในงานวิจัยส่วนนี้คณะวิจัยสนใจสารประกอบที่เรียกว่าไดมอนดอยด์ (diamondoid) ซึ่งมีสมบัติทางไฟฟ้าในเรื่องการปลดปล่อยอิเล็กตรอนที่ดีคล้ายกับเพชร [8] ในที่นี้คณะวิจัยพยายามสร้างฟิล์มบางของสารประกอบไดมอนดอยด์ (Adamantane, $C_{10}H_{16}$) ด้วยวิธี Chemical Vapor Deposition (CVD) และนำไปวัดโครงสร้างอิเล็กทรอนิกส์ด้วยเทคนิคโฟโตอิมิชชันสเปกโตรสโคปีแบบแยกแยะธาตุ (XPS) ซึ่งสามารถแยกประมาณของคาร์บอนที่อยู่ในรูป sp^2 และ sp^3 ทั้งนี้ยังพบว่าฟิล์มบางไดมอนดอยด์ดังกล่าวยังมีสมบัติปลดปล่อยอิเล็กตรอนได้ดีตามรูปที่ 8

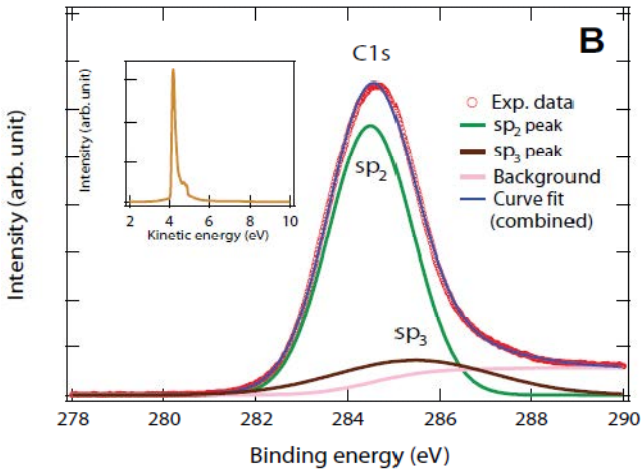

รูปที่ 8 โครงสร้างอิเล็กทรอนิกส์ของฟิล์มบางไดมอนดอยด์ที่พลังงานของคาร์บอน C1s สำหรับการแยกประมาณของคาร์บอนที่อยู่ในรูป sp^2 และ sp^3 และลักษณะของสมบัติปลดปล่อยอิเล็กตรอนที่ดี (ในรูปเล็ก)

เอกสารอ้างอิง

[1] S.Z. Butler *et al.*, ACS Nano 7, 2898-2926 (2013)

[2] K.F. Mak *et al.*, Phys. Rev. Lett. 105, 136805 (2010)

[3] T. Ekanapakul, et al., Nano Lett., 14, 1312 (2014).

[4] H. Yuan *et al.*, Nature Phys. 9, 563 (2013)

[5] J.M. Riley, et al., Nature Phys. 10, 835 (2014)

[6] W. Meevasana, et al. Nature Mater. 10, 114-118 (2011).

[7] P.D.C. King, et al., Nature Comms. 5, 3414 (2014).

[8] Y.L. Wang, et al. Science 316, 1460 (2007).

Output จากโครงการวิจัยที่ได้รับทุนจาก สกว.

1. ผลงานตีพิมพ์ในวารสารวิชาการนานาชาติ (ระบุชื่อผู้แต่ง ชื่อเรื่อง ชื่อวารสาร ปี เล่มที่ เลขที่ และหน้า) หรือผลงานตามที่คาดไว้ในสัญญาโครงการ

   1.1 Eknapakul T., King P.D.C., Asakawa M., Buaphet P., He R.-H., Mo S.-K., Takagi H., Shen K.M., Baumberger F., Sasagawa T., Jungthawan S., **Meevasana W.***, Electronic structure of a quasi-freestanding MoS2 monolayer, Nano Letters 14, 1312-1316 (2014) (5 citations, 11/6/2015) เอกสารที่ 1 ในภาคผนวก

1.2 Riley J.M., Mazzola F., Dendzik M., Michiardi M., Takayama T., Bawden L., Granerod C., Leandersson M., Balasubramanian T., Hoesch M., Kim T.K., Takagi H., **Meevasana W.**, Hofmann P., Bahramy M.S., Wells J.W., King P.D.C., Direct observation of spin-polarized bulk bands in an inversion-symmetric semiconductor, Nature Physics 10, 835-839 (2014) (4 citations, 11/6/2015) เอกสารที่ 2 ในภาคผนวก

1.3 King P.D.C., Walker S.M., Tamai A., De La Torre A., Eknapakul T., Buaphet P., Mo S.-K., **Meevasana W.**, Bahramy M.S., Baumberger F., Quasiparticle dynamics and spin-orbital texture of the SrTiO3 two-dimensional electron gas, Nature Communications 5, 3414 (2014) (7 citations, 11/6/2015) เอกสารที่ 3 ในภาคผนวก

หมายเหตุ นอกจาก 3 บทความข้างต้น ยังมีอีก 2 บทความตามรายละเอียดด้านล่างที่ข้าพเจ้าได้รับการสนับสนุนจาก สกว.-มทส. ตามสัญญาเลขที่ RSA5680052 นี้ ทั้งนี้ข้าพเจ้าจะแจ้งมาภายหลังเมื่อได้การตอบรับแล้ว อย่างไรก็ตามข้าพเจ้าขออนุญาตใช้เพียงผลงานวิจัยที่ 1.1 – 1.3 เพื่อใช้ในการปิดทุนตามเวลาที่ สกว. กำหนดไว้

- J. M. Riley, **W. Meevasana**, L. Bawden, M. Asakawa, T. Takayama, T. Eknapakul, T. K. Kim, M. Hoesch, S.-K. Mo, H. Takagi, T. Sasagawa, M. S. Bahramy, and P. D. C. King, Persistent negative electronic compressibility and tuneable spin splitting in WSe2, submitted to Nature Nanotechnology (2015)

- L. Bawden, J. M. Riley, C. H. Kim, R. Sankar, E. J. Monkman, D. E. Shai, H. I. Wei, E. Lochocki, J. W. Wells, **W. Meevasana**, T. K. Kim, M. Hoesch, Y. Ohtsubo, P. Le Fevre, C. J. Fennie, K. M. Shen, F. C. Chou, and P. D. C. King, Hierarchical spin-orbital polarisation of a giant Rashba system, submitted to Science Advances (2015)

2. การนำผลงานวิจัยไปใช้ประโยชน์

ข้อมูลโครงสร้างทางอิเล็กทรอนิกส์ของทั้ง MoS_2, WSe_2 และ $SrTiO_3$ สามารถใช้เป็นข้อมูลพื้นฐานในการเข้าใจสมบัติทางแม่เหล็กไฟฟ้าอันโดดเด่นซึ่งมีโอกาสใช้

ลักษณะพิเศษนี้ในการใช้ผลิตอุปกรณ์อิเล็กทรอนิกส์ที่มีความสามารถล้ำหน้าเทคโนโลยีที่มีอยู่ในปัจจุบัน

ทั้งนี้ผลงานวิจัยดังกล่าวได้ถูกตีพิมพ์อยู่ในวารสารวิชาการที่มี Impact Factor ทั้งสิ้น 3 เรื่องซึ่งอยู่ในฐานข้อมูล SCOPUS และมีการอ้างอิงในระดับนานาชาติแล้ว 16 ครั้ง ณ วันที่ 11 มิ.ย. 2558

3. อื่นๆ (เช่น ผลงานตีพิมพ์ในวารสารวิชาการในประเทศ การเสนอผลงานในที่ประชุมวิชาการ หนังสือ การจดสิทธิบัตร)

3.1 งานสัมมนา Advanced Light Source Users' Meeting 2014 บรรยายในเรื่อง Electronic structure modification at oxide surfaces via UV irradiation (invited talk) วันที่ 8 ต.ค. 2557 จัดโดย Advanced Light Source, Lawrence National Berkeley Lab. ในสหรัฐอเมริกา

3.2 งานสัมมนา The 1st International Conference on the Electronic Structure of Complex Quantum Matter and Microstructure เพื่อบรรยายในเรื่อง Electronic structure of a quasi-freestanding MoS2 monolayer วันที่ 30 พ.ค. – 2 มิ.ย. 2558 จัดโดย Fudan University, Shanghai ในประเทศจีน

3.3 บรรยายในเรื่อง Exploration of potential high-speed electronics with novel functionalities (plenary talk) ในงานประชุมวิชาการ Siam Physics Congress (SPC) 2014 จัดโดยสมาคมฟิสิกส์แห่งประเทศไทย วันที่ 26 - 29 มีนาคม 2557 ณ หอประชุมใหญ่ มหาวิทยาลัยเทคโนโลยีราชมงคลอีสาน จังหวัดนครราชสีมา

3.4 งาน ASEAN Workshop on Photoemission Electron Spectroscopy and Microscopy (AWPESM 2015) (invited talk) จัดโดยสถาบันวิจัยแสงซินโครตรอน 28 พ.ค. 2558 จ. นครราชสีมา ประเทศไทย

ภาคผนวก

เอกสารที่ 1

Eknapakul T., King P.D.C., Asakawa M., Buaphet P., He R.-H., Mo S.-K., Takagi H., Shen K.M., Baumberger F., Sasagawa T., Jungthawan S., **Meevasana W.***, Electronic structure of a quasi-freestanding MoS2 monolayer, Nano Letters 14, 1312-1316 (2014) (5 citations, 11/6/2015)

NANO LETTERS

Letter

pubs.acs.org/NanoLett

Electronic Structure of a Quasi-Freestanding MoS_2 Monolayer

T. Eknapakul,[†] P. D. C. King,*[,‡,§,∥] M. Asakawa,[⊥] P. Buaphet,[†] R.-H. He,[¶,□] S.-K. Mo,[¶] H. Takagi,[■,○] K. M. Shen,[§,∥] F. Baumberger,[●,△,‡] T. Sasagawa,[⊥] S. Jungthawan,[†,▲] and W. Meevasana*[,†,▲]

[†]School of Physics, Suranaree University of Technology, Nakhon Ratchasima, 30000, Thailand

[‡]SUPA, School of Physics and Astronomy, University of St. Andrews, St. Andrews, Fife KY16 9SS, United Kingdom

[§]Kavli Institute at Cornell for Nanoscale Science, Ithaca, New York 14853, United States

[∥]Laboratory of Atomic and Solid State Physics, Department of Physics, Cornell University, Ithaca, New York 14853, United States

[⊥]Materials and Structures Laboratory, Tokyo Institute of Technology, Kanagawa 226-8503, Japan

[¶]Advanced Light Source, Lawrence Berkeley National Laboratory, Berkeley, California 94720, United States

[□]Department of Physics, Boston College, Chestnut Hill, Massachusetts 02467, United States

[■]Department of Physics, University of Tokyo, Hongo, Tokyo 113-0033, Japan

[○]Magnetic Materials Laboratory, RIKEN Advanced Science Institute, Wako, Saitama 351-0198, Japan

[●]Département de Physique de la Matière Condensée, Universitée de Genève, 24 Quai Ernest-Ansermet, 1211 Genève 4, Switzerland

[△]Swiss Light Source, Paul Scherrer Institut, CH-5232 Villigen PSI, Switzerland

[▲]NANOTEC-SUT Center of Excellence on Advanced Functional Nanomaterials, Suranaree University of Technology, Nakhon Ratchasima 30000, Thailand

Supporting Information

ABSTRACT: Several transition-metal dichalcogenides exhibit a striking crossover from indirect to direct band gap semiconductors as they are thinned down to a single monolayer. Here, we demonstrate how an electronic structure characteristic of the isolated monolayer can be created at the surface of a bulk MoS_2 crystal. This is achieved by intercalating potassium in the interlayer van der Waals gap, expanding its size while simultaneously doping electrons into the conduction band. Our angle-resolved photoemission measurements reveal resulting electron pockets centered at the $\overline{K}$ and $\overline{K'}$ points of the Brillouin zone, providing the first momentum-resolved measurements of how the conduction band dispersions evolve to yield an approximately direct band gap of ∼1.8 eV in quasi-freestanding monolayer MoS_2. As well as validating previous theoretical proposals, this establishes a novel methodology for manipulating electronic structure in transition-metal dichalcogenides, opening a new route for the generation of large-area quasi-freestanding monolayers for future fundamental study and use in practical applications.

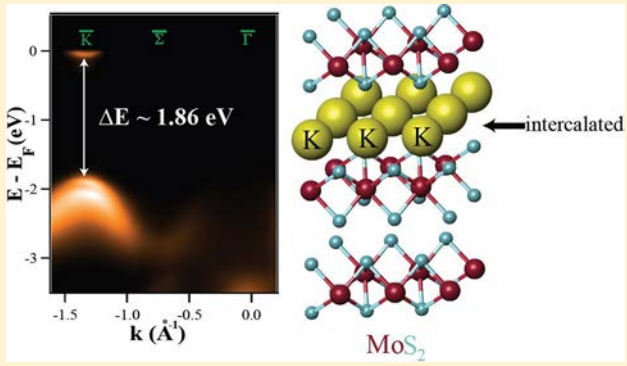

KEYWORDS: *Molybdenum disulfide (MoS_2), transition metal dichalcogenides (TMD), layered semiconductor, electronic structure, angle-resolved photoemission, van der Waals expansion*

Two-dimensional semiconductors fabricated from ultrathin transition-metal dichalcogenides (TMDs) hold enormous potential for novel optoelectronic device applications.[1] Exploiting weak van der Waals (vdW) interactions between neighboring chalcogen planes,[2,3] flakes of single (one chalcogen−metal−chalcogen unit, Figure 1a) or few-layer TMDs such as MoS_2 can be mechanically exfoliated, just as for isolating single monolayers of graphene.[4,5] The resulting quantum confinement and (for an individual monolayer) loss of inversion symmetry drives a dramatic reconstruction of the electronic structure, mediating a crossover from an indirect to a direct band gap[6,7] and strongly entangling the spin and valley degrees of freedom in this system.[8,9] The valley polarization can be controlled optically,[10,11] opening the door to a new generation of tunable valleytronic devices, while ultrathin MoS_2 has already been demonstrated as both an attractive channel[12] and barrier[13] layer for atomic-scale transistors.

Despite this progress, the momentum-resolved electronic structure of atomically thin TMDs remains almost completely unexplored in experiment to date, hampered by the small lateral dimensions of typical exfoliated flakes. While a recent spatial-

Received: November 19, 2013
Revised: February 19, 2014
Published: February 19, 2014

   dx.doi.org/10.1021/nl4042824 | *Nano Lett.* 2014, 14, 1312−1316

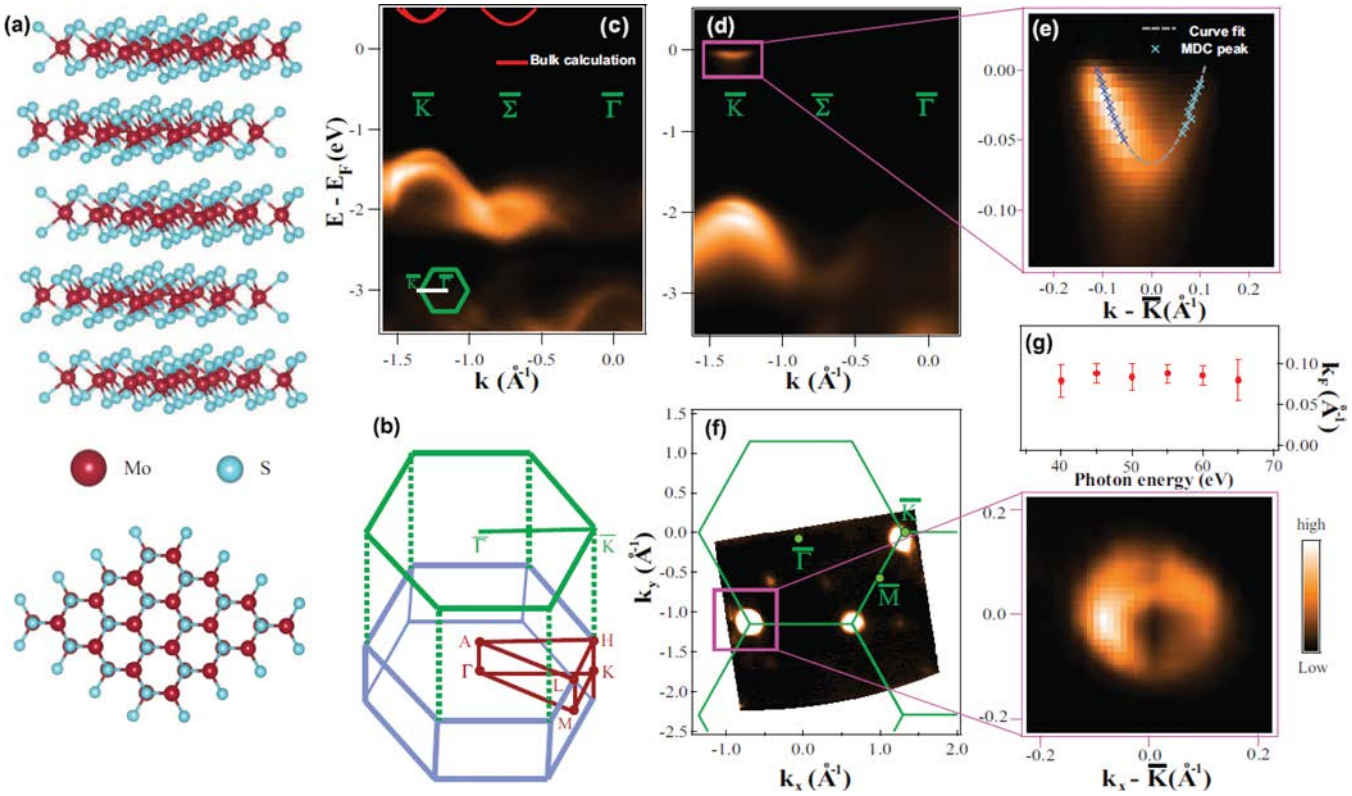

Figure 1. (a) Honeycomb structure of MoS_2, composed of stacked S−Mo−S units. (b) The resulting three-dimensional Brillouin zone and its projection onto the hexagonal surface Brillouin zone. (c,d) Valence band electronic structure measured along the $\bar{\Gamma}$−$\bar{K}$ direction for the pristine-cleaved surface and a potassium-dosed surface, respectively. The conduction band dispersions shown in panel (c) reproduce our bulk calculations from Figure 3(a), following an energy shift to correct the bulk band gap error in DFT. These indicate an indirect band gap, with the conduction-band minimum located at $\bar{\Sigma}$. Following potassium dosing, an electron pocket is found at $\bar{K}$, shown magnified in (e). (f) Equivalent Fermi surface pockets are found at each $\bar{K}$ and $\bar{K}'$ point of the surface Brillouin zone with weak additional spectral weight indicating the presence of a secondary (higher) band minimum along the $\bar{\Gamma}$−$\bar{K}$ line at the position of the global conduction-band minimum in bulk; the integration window of the map is set to be 50 meV around the Fermi energy. The $\bar{K}$-centered Fermi pockets are nondispersive in k_z, as shown by photon-energy independence of their extracted Fermi wavevectors (g), measured from a different sample with lower potassium coverage, and therefore smaller k_F, than in (d−f).

imaging angle-resolved photoemission (ARPES) study was able to map the occupied valence band dispersions of micrometer-scale flakes of monolayer MoS_2,[14] the key question of the conduction band dispersions and their momentum-space locations remained inaccessible. Furthermore, the experimental resolution was not sufficient to discern subtle but important details of its electronic structure such as spin−orbit splittings.

To aid such fundamental studies, as well as for ultimate applications of these compounds, new schemes are required to synthesize large-area monolayer TMDs. Motivated by recent progress on the creation of quasi-freestanding epitaxial monolayers of graphene at the surface of SiC(0001)[15] and metallic substrates,[16] and the new insights gained from their spectroscopic study,[17] here we report the first characterization of the electronic structure of a quasi-freestanding monolayer of MoS_2. This is created at the surface of bulk MoS_2 by intercalating potassium into the interlayer vdW gap. Simultaneously, this dopes electrons into the conduction band. Our subsequent ARPES measurements reveal electron Fermi surface pockets formed from conduction bands with their minima located at the $\bar{K}$ and $\bar{K}'$ points of the Brillouin zone. This is in agreement with theoretical expectations for an isolated monolayer, but in contrast to the bulk electronic structure, and permits the first direct measurement of the conduction band dispersions of monolayer-like MoS_2, revealing an unexpectedly large effective mass. These findings are of key importance for understanding both electrical transport and optical transitions in monolayer MoS_2, as well as establishing a new route for the creation of large-area supported monolayers of TMDs.

Single crystals of 2H-MoS_2 were grown using the flux method and cleaved in ultrahigh vacuum at a pressure better than 4×10^{-11} Torr to reveal a pristine (0001) surface. Their electronic structure was measured using ARPES, performed at beamline 10.0.1 of the Advanced Light Source, U.S.A., using photon energies between 40 and 65 eV and a Scienta R4000 hemispherical electron analyzer. The energy and angular resolutions were set at 10−20 meV and 0.3°, respectively, and the sample temperature was maintained at 20 K throughout the experiment. Measurements were performed immediately after the cleave, as well as following the deposition of potassium on to the sample surface from a properly outgassed SAES getter source. Density functional theory (DFT) calculations were performed using the VASP code,[18] employing the Perdew, Burke, and Erzenhoff (PBE)[19] exchange-correlation function implemented within the projector augmented wave method.[20] The cutoff energy was set at 600 eV and a Γ-centered 24 × 24 × 5 Monkhorst-Pack k-mesh was used for the Brillouin zone integrations. van der Waals corrections to the dispersions were included within the DFT + D2 approach of Grimme.[21]

The electronic structure measured along the $\bar{\Gamma}$−$\bar{K}$ direction of the surface Brillouin zone is shown for the pristine cleaved

dx.doi.org/10.1021/nl4042824 | Nano Lett. 2014, 14, 1312−1316

sample in Figure 1c. As expected for semiconducting MoS_2, the chemical potential lies within the band gap, and there is no spectral weight at the Fermi level. We observe a clear splitting in energy of the valence bands at the $\bar{K}$ point of ~170 ± 12 meV (see Supporting Information for more detail), a direct signature of both interlayer interactions and spin−orbit coupling in this compound. This is in quantitative agreement with both quasiparticle self-consistent GW (QSGW) calculations[22] and the energy splitting of so-called A and B exciton peaks in optical spectroscopy from bulk MoS_2.[23] After depositing potassium at the surface, the valence bands move to higher binding energy, consistent with electron transfer from potassium to the MoS_2, corroborating recent reports from transport of efficient *n*-type doping by potassium deposition on few-layer TMDs.[24] We find sufficient electron donation to move the Fermi level into the conduction band (Figure 1d,e). The resulting Fermi surface comprises circular electron pockets at each $\bar{K}$ ($\bar{K}'$) point of the Brillouin zone as well as weak spectral weight associated with secondary band minima approximately midway along the $\bar{\Gamma}$−$\bar{K}$ ($\bar{\Gamma}$−$\bar{K}'$) directions (denoted here as $\bar{\Sigma}$). Strikingly, these measurements reveal that the conduction band minima (CBM) are located at the $\bar{K}$ ($\bar{K}'$) points of the Brillouin zone. This is not the case for the bulk electronic structure where the CBM are known to lie at $\bar{\Sigma}$ (Figure 1c), that is, away from high symmetry points,[3,25−27] but is representative of theoretical expectations for monolayer MoS_2,[26,28] a point we return to below.

From fitting the peak positions extracted from momentum distribution curves (MDCs) to a parabolic effective mass model, we estimate the effective mass of the lowest electron pocket as 0.67 ± 0.08m_e. This relatively high value, larger than predicted by QSGW calculations,[22] may help explain the modest mobilities that have been achieved to date in monolayer MoS_2 transistors.[29] Within experimental error, we find that this band does not disperse as we vary the photon energy between 40 and 65 eV (Figure 1g), a change of wavevector along the surface normal, k_z, by approximately 1.5 Brillouin zones. This indicates that the electron pockets formed are two-dimensional. Moreover, while weak spectral weight can be seen right at the Fermi level at $\bar{\Sigma}$ (evident in the Fermi surface map of Figure 1f and in the data of Figure 1d when plotted with enhanced color contrast, as shown in Figure S2), these remain well above the $\bar{K}$ band minimum for all values of k_z. This confirms that the CBM remains at $\bar{K}$ throughout the Brillouin zone, consistent with the expected electronic structure of monolayer MoS_2. We estimate the surface charge density from the Luttinger area of these measured, two-dimensional, Fermi surface pockets at $\bar{K}$ ($\bar{K}'$) as $n_{2D} = g_v k_F^2/2\pi = 3.8 \pm 0.6 \times 10^{13}$ cm^{-2}, where $g_v = 2$ is the valley multiplicity and $k_F = 0.11 \pm 0.01$ Å^{-1} the measured Fermi wavevector, corresponding to ~0.03 ± 0.005 electrons per surface unit cell.

Although the valence band has weak spectral weight at the zone center due to suppressed transition matrix elements,[30] we can still estimate from the energy-distribution curves (EDC) of our ARPES data that the onset of the valence band at the $\bar{\Gamma}$ point lies no higher than 50−100 meV above that at the $\bar{K}$ point (see Supporting Information for more detail), indicating an approximately direct nature of the band gap here, as for isolated monolayer MoS_2.[6,7] The direct band gap at the $\bar{K}$ point extracted from the peak-to-peak conduction/valence band separation in EDCs is 1.86 ± 0.02 eV, as shown in Figure 1d and in excellent agreement with the direct band gap of monolayer MoS_2 of 1.88 eV estimated from photoluminescence by Mak et al.[7] From EDC fits to our measured dispersions (see Figure 3f), we extract an effective mass for the highest valence band states at $\bar{K}$ to be 0.6 ± 0.08m_e. This is very similar to the conduction band effective mass at $\bar{K}$ discussed above, leading to a large joint density of states for optical transitions between the band edges. This is likely important to aid understanding and optimizing the high sensitivity of atomically thin MoS_2 based photodetectors,[31] as well as enabling the efficient optical generation of valley-polarized carrier populations in monolayer MoS_2,[9−11] key to proposed optoelectronic and valleytronic applications of this material.

Together, these findings strongly support that the electronic structure we are probing here is characteristic of monolayer rather than bulk MoS_2. To uncover the origins of this we combine chemical analysis from X-ray photoemission spectroscopy (XPS) with DFT calculations, as shown in Figure 2. A

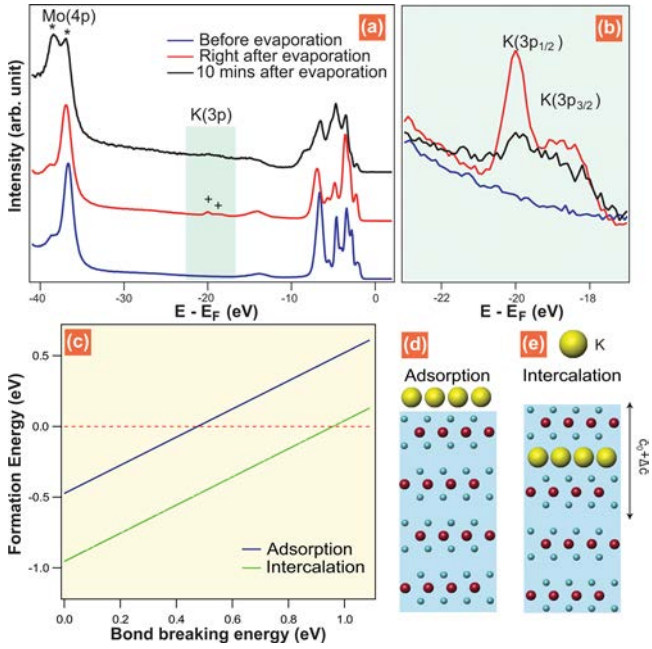

Figure 2. (a) XPS spectra of MoS_2 taken before and after potassium evaporation. (b) Magnified view of the potassium K 3p core-level photoemission. Measurements are presented for a pristine cleaved sample (blue line), immediately following potassium evaporation for 900 s (red line), and for the same sample after a further 10 min waiting time (black line). (c) Formation energies for placing a monolayer of potassium on-top of bulk MoS_2 [adsorption, (d)] or intercalated within the first vdW gap [intercalation, (e)], as derived from supercell DFT calculations.

wide binding energy range from 0 to 40 eV includes the MoS_2 valence bands and shallow core levels of molybdenum (Mo 4p, $E_B \approx 35-40$ eV) and potassium (K 3p, $E_B \approx 18-21$ eV). For the freshly cleaved sample, there is no potassium signal as expected, and sharp valence band and Mo 4p features are observed. With evaporation of potassium, these shift to higher binding energy, a result of the electron doping, and a clear K 3p peak emerges. From the relative intensity of the Mo and K core levels, we estimate the surface coverage of potassium to be 0.06 atoms per unit cell of MoS_2. Intriguingly, over a time scale of ~10 min, the intensity of this potassium core-level peak is strongly diminished, and we additionally observe a partial shift of spectral weight from both the K 3p and Mo 4p peaks to higher binding energy, indicating a change in the local

dx.doi.org/10.1021/nl4042824 | Nano Lett. 2014, 14, 1312−1316

environment of the potassium atoms. Desorption seems unlikely at the deposition and measurement temperature of 20 K, and the conduction band is degenerately doped after this transition. Therefore, we attribute these changes in the XPS spectra to the intercalation of potassium into the vdW gap between neighboring MoS_2 units. This is fully supported by our DFT calculations (Figure 2c), which reveal a significantly lower formation energy for potassium to be intercalated in the first vdW gap (Figure 2e) rather than to be adsorbed on the surface (Figure 2d).

Intercalating potassium into this vdW gap would be expected to increase the interlayer spacing, and we propose that this drives a crossover from a bulk- to monolayer-like electronic structure in our samples.[32] Our DFT calculations (Figure 3) reveal just such a transition with increasing c/a ratio (i.e., expansion of the vdW gap) of a bulk MoS_2 unit cell. These calculations neglect spin−orbit interactions, allowing us to monitor the energy splitting of the valence band maxima at $\bar{K}$ as a metric of the strength of interlayer interactions in the material (summarized in Figure 3e). With increasing c/a ratio, this splitting is reduced to near zero, indicating a negligible coupling between neighboring MoS_2 units along the z axis for c/a ratios above ∼4.9 (vdW gaps larger than 4.69 Å). The effects of this are much more dramatic close to $\bar{\Gamma}$ and $\bar{\Sigma}$, where the electronic states have significant S 2p character in contrast to the almost completely Mo d-derived character of the $\bar{K}$-point states. Consequently, the interlayer interaction in bulk is significantly stronger, leading to much larger energy splittings.[33] The weakening of the interlayer coupling by the vdW gap expansion here drives a large reduction of these energy splittings, eventually resulting in an inversion of the ordering of band extrema at $\bar{K}$ and along the $\bar{\Gamma}$−$\bar{K}$ line.

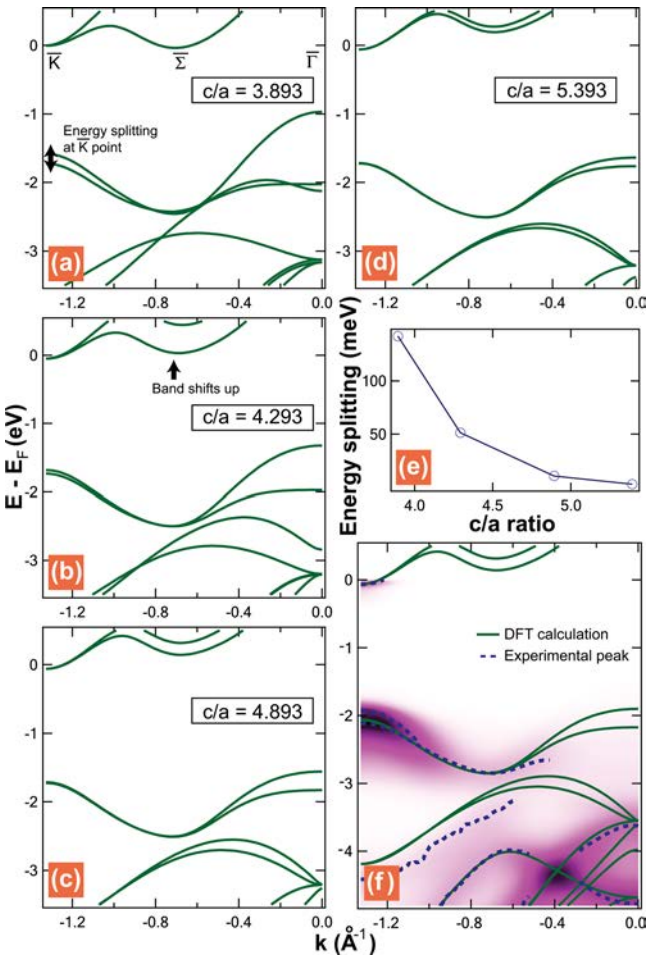

Figure 3. (a−d) DFT band structure calculations for MoS_2 with different interlayer spacings, indicated by the ratio between out-of-plane and in-plane lattice constants (c/a). (e) Energy splitting of the valence band maxima at $\bar{K}$. In the absence of spin−orbit interactions, these are indicative of the relative strength of interlayer interactions. (f) Comparison between our measured ARPES data, extracted dispersions from fitting EDCs, and the theoretical calculations for c/a = 4.893, showing good agreement. The total magnitude of the energy gap, underestimated due to the standard LDA band gap error, is adjusted to better match our experimental valence band dispersions.

Thus, for sufficient increase in interlayer spacing, each MoS_2 unit effectively becomes an isolated monolayer. We find good agreement between our theoretical and experimental dispersions here for an increase in the c/a ratio of ∼25%. While large, we note that vdW gaps expanded as much as 30% have been reported in bulk potassium-intercalated MoS_2.[34] A similar increase of the first vdW gap below the surface therefore seems reasonable here, leading to an isolated quasi-freestanding monolayer at the surface of a bulk MoS_2 crystal. Our work also suggests that superconductivity in alkali metal-doped MoS_2[34] with similar vdW gap sizes as for the surface here emerges from an electronic structure characteristic of a series of stacked monolayers rather than bulklike MoS_2. This will likely be key to understanding a putative unconventional dome of superconductivity formed from both electrically gated and intercalated MoS_2 samples.[35]

Finally, we note that even for the monolayer-like electronic structure we observe here, we still find a splitting in the valence bands at the $\bar{K}$-point (Figure 1d) of 176 ± 12 meV (see Supporting Information for more detail). This is comparable to both monolayer electronic structure calculations[22,28] and exciton peak splittings in photoluminescence from monolayer MoS_2,[6] which suggest splittings around 150 meV. The persistent splitting observed here, even with small interlayer interactions, reflects a significant influence of spin−orbit coupling on the monolayer-like electronic structure, not considered in our DFT calculations above, but permitted by the broken inversion symmetry of the surface monolayer. This confirms the strong potential of MoS_2 and related compounds for spintronic applications.[36] Moreover, it suggests that the prospects for valleytronics offered by monolayer MoS_2[8−11] should also be realized in the quasi-freestanding monolayer created here. Unlike mechanical exfoliation, however, our methodology allows the possibility to continuously tune the electronic structure from bulklike to monolayer-like by controlling the vdW gap expansion by intercalating different quantities of potassium or atoms of different sizes. Moreover, it raises the prospect to reversibly drive this crossover in TMDs by sequential intercalation and deintercalation, as has recently been achieved for graphene.[37] Together, our work establishes intercalation at the surface of bulk TMDs as an efficient route to generate large-area quasi-freestanding monolayers for use in advanced fundamental study and potential practical applications of MoS_2 and other atomic-scale transition-metal dichalcogenides.

■ ASSOCIATED CONTENT

Supporting Information

Descriptions of the suppression of spectral intensity close to the zone center and the extraction of splitting in energy are

dx.doi.org/10.1021/nl4042824 | Nano Lett. 2014, 14, 1312−1316

provided. This material is available free of charge via the Internet at http://pubs.acs.org.

AUTHOR INFORMATION

Corresponding Authors

*E-mail: (P.D.C.K.) philip.king@st-andrews.ac.uk.
*E-mail: (W.M.) worawat@g.sut.ac.th.

Notes

The authors declare no competing financial interest.

ACKNOWLEDGMENTS

This work was supported by Thailand Research Fund, Suranaree University of Technology (TRF Grant RSA5680052), Office of Higher Education Commissions under NRU project, the U.K. EPSRC (EP/I031014/1) and ERC (207901). T.E. acknowledges DPST for financial support. P.D.C.K. acknowledges support from the Royal Society through a University Research Fellowship. K.M.S. and P.D.C.K. acknowledge support from the Office of Naval Research (Grant No. N00014-12-1-0791). S.J. acknowledges support from NANOTEC, NSTDA, Thailand, through its program of Center of Excellence Network. The Advanced Light Source is supported by the Director, Office of Science, Office of Basic Energy Sciences, of the U.S. Department of Energy under Contract No. DE-AC02-05CH11231. We also gratefully acknowledge K.F. Mak and T. Cheiwchanchamnangij for useful discussions.

REFERENCES

(1) Wang, Q. H.; Kalantar-Zadeh, K.; Kis, A.; Coleman, J. N.; Strano, M. S. *Nat. Nanotechnol.* **2012**, *7*, 699.
(2) Mattheiss, L. F. *Phys. Rev. B* **1973**, *8*, 3719.
(3) Coehoorn, R.; Haas, C.; Dijkstra, J.; Flipse, C. J. F. *Phys. Rev. B* **1987**, *35*, 6195.
(4) Novoselov, K. S.; Jiang, D.; Schedin, F.; Booth, T. J.; Khotkevich, V. V.; Morozov, S. V.; Geim, A. K. *Proc. Natl. Acad. Sci. U.S.A.* **2005**, *102*, 10454.
(5) Coleman, J. N.; Lotya, M.; O'Neill, A.; Bergin, S. D.; King, P. J.; Khan, U.; Young, K.; Gaucher, A.; De, S.; Smith, R. J.; Shvets, I. V.; Arora, S. K.; Stanton, G.; Kim, H.-Y.; Lee, K.; Kim, G. T.; Duesberg, G. S.; Hallam, T.; Boland, J. J.; Wang, J. J.; Donegan, J. F.; Grunlan, J. C.; Moriarty, G.; Shmeliov, A.; Nicholls, R. J.; Perkins, J. M.; Grieveson, E. M.; Theuwissen, K.; McComb, D. W.; Nellist, P. D.; Nicolosi, V. *Science* **2011**, *331*, 568.
(6) Mak, K. F.; Lee, C.; Hone, J.; Shan, J.; Heinz, T. F. *Phys. Rev. Lett.* **2010**, *105*, 136805.
(7) Splendiani, A.; Sun, L.; Zhang, Y.; Li, T.; Kim, J.; Chim, C.-Y.; Galli, G.; Wang, F. *Nano Lett.* **2010**, *10*, 1271.
(8) Xiao, D.; Liu, G.-B.; Feng, W.; Xu, X.; Yao, W. *Phys. Rev. Lett.* **2012**, *108*, 196802.
(9) Cao, T.; Wang, G.; Han, W.; Ye, H.; Zhu, C.; Shi, J.; Niu, Q.; Tan, P.; Wang, E.; Liu, B.; Feng, J. *Nat. Commun.* **2012**, *3*, 887.
(10) Zeng, H.; Dai, J.; Yao, W.; Xiao, D.; Cui, X. *Nat. Nanotechnol.* **2012**, *7*, 490.
(11) Mak, K. F.; He, K.; Shan, J.; Heinz, T. F. *Nat. Nanotechnol.* **2012**, *7*, 494.
(12) Radisavljevic, B.; Radenovic, A.; Brivio, J.; Giacometti, V.; Kis, A. *Nat. Nanotechnol.* **2011**, *6*, 147.
(13) Britnell, L.; Gorbachev, R. V.; Jalil, R.; Belle, B. D.; Schedin, F.; Mishchenko, A.; Georgiou, T.; Katsnelson, M. I.; Eaves, L.; Morozov, S. V.; Peres, N. M. R.; Leist, J.; Geim, A. K.; Novoselov, K. S.; Ponomarenko, L. A. *Science* **2012**, *335*, 947.
(14) Jin, W.; Yeh, P.-C.; Zaki, N.; Zhang, D.; Sadowski, J. T.; Al-Mahboob, A.; Zande, A. M.; Chenet, D. A.; Dadap, J. I.; Herman, I. P.; Sutter, P.; Hone, J.; Osgood, R. M. *Phys. Rev. Lett.* **2013**, *111*, 106801.
(15) Riedl, C.; Coletti, C.; Iwasaki, T.; Zakharov, A. A.; Starke, U. *Phys. Rev. Lett.* **2009**, *103*, 246804.
(16) Varykhalov, A.; Sánchez-Barriga, J.; Shikin, A. M.; Biswas, C.; Vescovo, E.; Rybkin, A.; Marchenko, D.; Rader, O. *Phys. Rev. Lett.* **2008**, *101*, 157601.
(17) Bostwick, A.; Speck, F.; Seyller, T.; Horn, K.; Polini, M.; Asgari, R.; MacDonald, A. H.; Rotenberg, E. *Science* **2010**, *328*, 999.
(18) Kresse, G.; Furthmüller, J. *Comput. Mater. Sci.* **1996**, *6*, 15.
(19) Perdew, J. P.; Burke, K.; Ernzerhof, M. *Phys. Rev. Lett.* **1996**, *77*, 3865.
(20) Blöchl, P. E. *Phys. Rev. B* **1994**, *50*, 17953.
(21) Grimme, S. *J. Comput. Chem.* **2006**, *27*, 1787.
(22) Cheiwchanchamnangij, T.; Lambrecht, W. R. L. *Phys. Rev. B* **2012**, *85*, 205302.
(23) Beal, A. R.; Hughes, H. P. *J. Phys. C* **1979**, *12*, 881.
(24) Fang, H.; Tosun, M.; Seol, G.; Chang, T. C.; Takei, K.; Guo, J.; Javey, A. *Nano Lett.* **2013**, *13*, 1991.
(25) Kuc, A.; Zibouche, N.; Heine, T. *Phys. Rev. B* **2011**, *83*, 245213.
(26) Ellis, J. K.; Lucero, M. J.; Scuseria, G. E. *Appl. Phys. Lett.* **2011**, *99*, 261908.
(27) Alexiev, V.; Prins, R.; Weber, T. *Phys. Chem. Chem. Phys.* **2000**, *2*, 1815.
(28) Zhu, Z. Y.; Cheng, Y. C.; Schwingenschlögl, U. *Phys. Rev. B* **2011**, *84*, 153402.
(29) Zhang, Y.; Ye, J.; Matsuhashi, Y.; Iwasa, Y. *Nano Lett.* **2012**, *12*, 1136.
(30) Damasceli, A.; Hussain, Z.; Shen, Z. X. *Rev. Mod. Phys.* **2003**, *75*, 473541.
(31) Lopez-Sanchez, O.; Lembke, D.; Kayci, M.; Radenovic, A.; Kis, A. *Nat. Nanotechnol.* **2013**, *8*, 497.
(32) Previous low-energy electron diffraction − Mrstik, B. J.; Kaplan, R.; Reinecke, T. L. *Phys. Rev. B* **1977**, *15*, 897. − and ion scattering − Kadowaki, Y.; Aika, K. *Surf. Sci.* **1993**, *287*, 396 − have revealed a small decrease in the spacing between the first and second MoS_2 unit at the surface of bulk cleaved MoS_2, and so we rule out that this vdW expansion exists at the freshly cleaved surface..
(33) Cappelluti, E.; Roldán, R.; Silva-Guillén, J. A.; Ordejón, P.; Guinea, F. *Phys. Rev. B* **2013**, *88*, 075409.
(34) Somoano, R. B.; Hadek, V.; Rembaum, A. *J. Chem. Phys.* **1973**, *58*, 697.
(35) Ye, J. T.; Zhang, Y. J.; Akashi, R.; Bahramy, M. S.; Arita, R.; Iwasa, Y. *Science* **2012**, *338*, 1193.
(36) Morpurgo, A. F. *Nat. Phys.* **2013**, *9*, 532.
(37) Larciprete, R.; Ulstrup, S.; Lacovig, P.; Dalmiglio, M.; Bianchi, M.; Mazzola, F.; Hornekær, L.; Orlando, F.; Baraldi, A.; Hofmann, P.; Lizzit, S. *ACS Nano* **2012**, *6*, 9551.

เอกสารที่ 2

Riley J.M., Mazzola F., Dendzik M., Michiardi M., Takayama T., Bawden L., Granerod C., Leandersson M., Balasubramanian T., Hoesch M., Kim T.K., Takagi H., **Meevasana W.**, Hofmann P., Bahramy M.S., Wells J.W., King P.D.C., Direct observation of spin-polarized bulk bands in an inversion-symmetric semiconductor, Nature Physics 10, 835-839 (2014) (4 citations, 11/6/2015))

nature physics

LETTERS

PUBLISHED ONLINE: 5 OCTOBER 2014 | DOI: 10.1038/NPHYS3105

Direct observation of spin-polarized bulk bands in an inversion-symmetric semiconductor

J. M. Riley[1], F. Mazzola[2], M. Dendzik[3], M. Michiardi[3], T. Takayama[4,5], L. Bawden[1], C. Granerød[2], M. Leandersson[6], T. Balasubramanian[6], M. Hoesch[7], T. K. Kim[7], H. Takagi[4,5], W. Meevasana[8,9], Ph. Hofmann[3], M. S. Bahramy[10,11], J. W. Wells[2] and P. D. C. King[1]*

Methods to generate spin-polarized electronic states in non-magnetic solids are strongly desired to enable all-electrical manipulation of electron spins for new quantum devices[1]. This is generally accepted to require breaking global structural inversion symmetry[1–5]. In contrast, here we report the observation from spin- and angle-resolved photoemission spectroscopy of spin-polarized bulk states in the centrosymmetric transition-metal dichalcogenide WSe_2. Mediated by a lack of inversion symmetry in constituent structural units of the bulk crystal where the electronic states are localized[6], we show how spin splittings up to ∼0.5 eV result, with a spin texture that is strongly modulated in both real and momentum space. Through this, our study provides direct experimental evidence for a putative locking of the spin with the layer and valley pseudospins in transition-metal dichalcogenides[7,8], of key importance for using these compounds in proposed valleytronic devices.

The powerful combination of inversion symmetry $[E(\mathbf{k},\uparrow)=E(-\mathbf{k},\uparrow)]$ with time-reversal symmetry $[E(\mathbf{k},\uparrow)=E(-\mathbf{k},\downarrow)]$ ensures that electronic states of non-magnetic centrosymmetric materials must be doubly spin-degenerate. If inversion symmetry is broken, however, relativistic spin–orbit interactions can induce a momentum-dependent spin splitting via an effective magnetic field imposed by spatially-varying potentials. If the resulting spin polarizations can be controllably created and manipulated, they hold enormous promise to enable a range of new quantum technologies. These include routes towards electrical control of spin precession for spin-based electronics[1,9], new ways to engineer topological states[10,11] and possible hosts of Majorana fermions for use in quantum computation[5]. There are two generally accepted methods for stabilizing spin-polarized states without magnetism, both exploiting breaking of global inversion symmetry. Structural inversion asymmetry can be created in a centrosymmetric host by imposing an electrostatic potential gradient, for example within an asymmetric quantum well, leading to Rashba-split[12] states localized at surfaces or interfaces[13–16]. Alternatively, a lack of global inversion symmetry in the unit cell can mediate spin splitting of the bulk electronic states, either through a Dresselhaus-type interaction[17], or a recently discovered bulk form of the Rashba effect[4,18].

Here, we present direct experimental evidence that 2*H*-WSe_2, a material which retains bulk inversion symmetry, nonetheless exhibits a large spin polarization of its bulk electronic states. This layered compound is composed of stacked Se–W–Se planes (Fig. 1a), each of which contains an in-plane net dipole moment which is proposed to lead to a strong spin–valley coupling for an isolated monolayer[19–21]. The bulk unit cell contains two such monolayers, stacked in a staggered 'AB' configuration, restoring inversion symmetry and necessitating spin degeneracy of the bulk electronic states. Nevertheless, combining spin- and angle-resolved photoemission spectroscopy (ARPES) with electronic structure calculations, we observe a large layer- and momentum-dependent spin polarization of these bulk bands.

We first summarize the bulk electronic structure of WSe_2 (Fig. 1). The material is known to be a semiconductor, consistent with our experimental observations, where we find the Fermi level located within the bandgap. We find the band extrema of the valence bands at Γ and K to be almost degenerate[22], but here can resolve that the valence band maximum is located at the bulk Γ point, with significant dispersion of these zone-centre states along the surface normal (k_z) direction (Fig. 1c,e). Our measured band dispersions are in excellent agreement with those calculated from density functional theory (DFT; see also Supplementary Fig. 1), confirming that we are probing the bulk electronic states of WSe_2. The broad total bandwidth of more than 4 eV of the cosine-like upper valence bands along Γ–A reflects the spatially extended nature of W 5*d* and Se 5*p* orbitals from which these states predominantly derive.

As well as these dispersive states we find a series of quasi-two-dimensional states, predominantly of planar $d_{x^2-y^2}$, d_{xy} and $p_{x/y}$ orbital character. The small overlap of these orbitals along the *z* direction, combined with suppressed interlayer hopping due to spin–orbit coupling[7], results in minimal dispersion along k_z, while their extended nature in-plane ensures significant dispersion throughout the surface Brillouin zone (Fig. 1d). The lowest binding energy two-dimensional states form a pair of hole-like bands centred at the Brillouin zone corners, contributing concentric, approximately circular pockets near the band top. These become trigonally warped as they grow in size with increasing binding energy, eventually merging with the zone-centre bands to form

[1]SUPA, School of Physics and Astronomy, University of St Andrews, St Andrews, Fife KY16 9SS, UK, [2]Department of Physics, Norwegian University of Science and Technology (NTNU), N-7491 Trondheim, Norway, [3]Department of Physics and Astronomy, Interdisciplinary Nanoscience Center (iNANO), Aarhus University, 8000 Aarhus C, Denmark, [4]Department of Physics, University of Tokyo, Hongo, Tokyo 113-0033, Japan, [5]Max Planck Institute for Solid State Research, 70569 Stuttgart, Germany, [6]MAX IV Laboratory, Lund University, P. O. Box 118, 221 00 Lund, Sweden, [7]Diamond Light Source, Harwell Campus, Didcot OX11 0DE, UK, [8]School of Physics, Suranaree University of Technology, Nakhon Ratchasima, 30000, Thailand, [9]NANOTEC-SUT Center of Excellence on Advanced Functional Nanomaterials, Suranaree University of Technology, Nakhon Ratchasima 30000, Thailand, [10]Quantum-Phase Electronics Center and Department of Applied Physics, The University of Tokyo, Tokyo 113-8656, Japan, [11]RIKEN center for Emergent Matter Science (CEMS), Wako 351-0198, Japan. *e-mail: philip.king@st-andrews.ac.uk

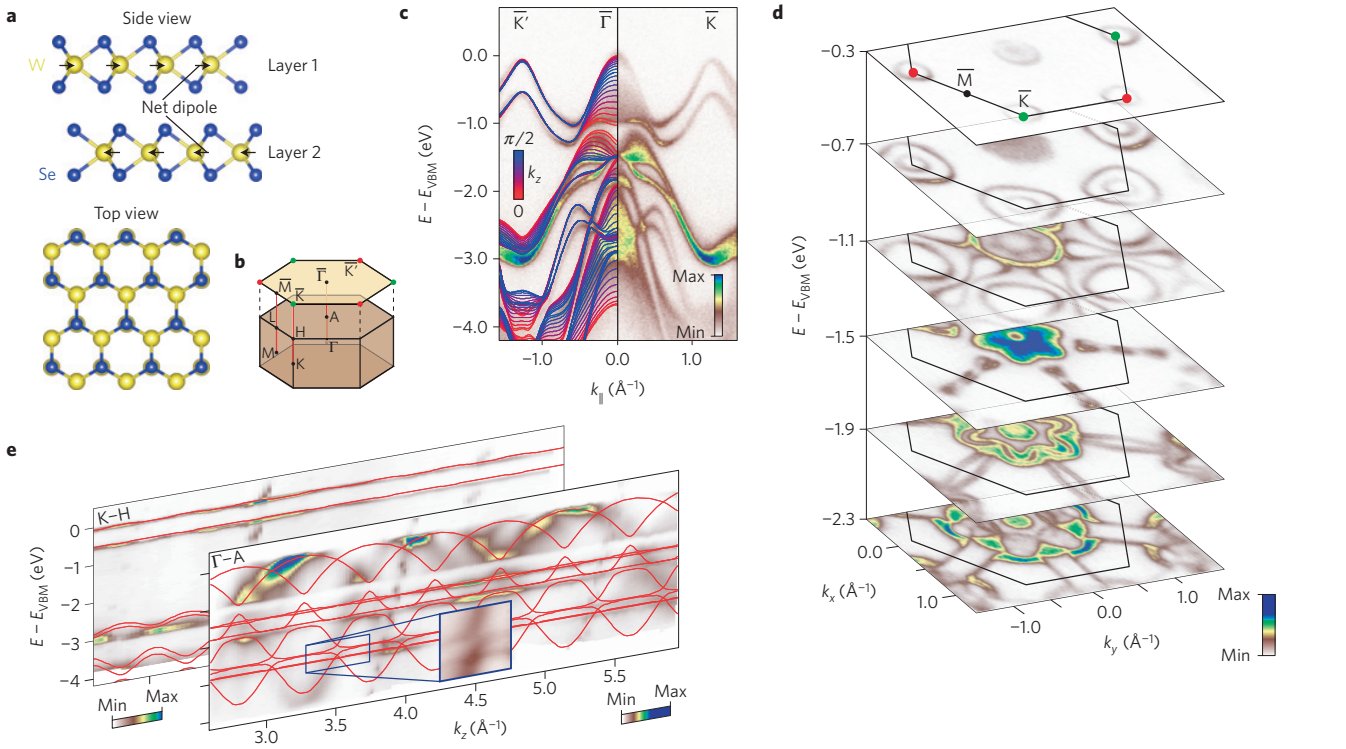

Figure 1 | Bulk electronic structure of WSe_2. a, Side and top views of the bulk crystal structure of WSe_2. The unit cell contains two Se–W–Se units in which there is a net in-plane dipole pointing to the right and left, respectively. **b**, Corresponding bulk and surface Brillouin zone. **c**,**d**, ARPES measurements ($h\nu = 125$ eV, $T = 30$ K) of the electronic structure along the $\overline{K}'$-$\overline{\Gamma}$-$\overline{K}$ direction (**c**) and isoenergy contours throughout the surface Brillouin zone (**d**) reveal sharply-defined bands (for example, the upper valence bands at $\overline{K}$) with significant in-plane dispersion, indicative of two-dimensional electronic states. We also observe broader 'filled-in' pockets of spectral weight characteristic of three-dimensional states, where the finite k_z resolution of ARPES leads to broadening. **e**, We directly confirm this absence or presence, respectively, of significant k_z dispersion from photon-energy-dependent ARPES measurements (Methods and Supplementary Fig. 1). Our measured electronic structure is in excellent agreement with that calculated from density functional theory (solid lines in **c**,**e**), confirming that we are probing the bulk electronic states of WSe_2.

bone-shaped pockets centred at $\overline{M}$. The large splitting of ~0.5 eV of the top of these bands at $\overline{K}$ signifies the strong atomic spin–orbit interaction in this compound, which is further reflected by our observation of hybridization gaps, for example between two- and three-dimensional states along the Γ–A line (Fig. 1e). Despite such strong spin–orbit coupling, we stress that all states remain spin-degenerate in our calculations, as expected from the bulk inversion symmetry of the crystal.

Intriguingly, however, our spin-resolved photoemission measurements reveal a strong spin polarization of the upper pair of valence band states at the $\overline{K}$ point of the Brillouin zone (Fig. 2). The measured polarization is entirely out of the surface plane within experimental error, with up (down) orientation for the upper (lower) valence band, respectively. From fitting the measured energy distribution curves (EDCs, described in Methods), we estimate the magnitude of the spin polarization to exceed 90%, suggestive of an almost fully spin-polarized band. Moreover, the signs of all polarizations are reversed at the $\overline{K}' = -\overline{K}$ point, confirming that time-reversal symmetry remains unbroken, and thus there is no net magnetic moment. This indicates a non-magnetic origin of the observed spin polarization, seemingly at odds with the centrosymmetric nature of the bulk crystal structure (Fig. 1a). We attribute this to the local inversion asymmetry of individual WSe_2 layers, leading to spin-polarized states whose texture is strongly modulated in both real and momentum space despite the global inversion symmetry of the unit cell. For these quasi-two-dimensional bands around $\overline{K}$, our calculations reveal that the electronic wavefunctions are almost completely localized on individual Se–W–Se layers of the bulk crystal. This is consistent with a spin–orbit-mediated suppression of interlayer hopping predicted at the $\overline{K}$ point for bilayer WSe_2, which was proposed to lead to a strong coupling of the real spin with the layer pseudospin[7]. Such spin–layer locking was subsequently attributed as the origin of characteristic circularly and linearly polarized photoluminescence from bilayer WSe_2 (ref. 8).

As in the bilayer, with the electronic wavefunctions localized on a single Se–W–Se layer (half of the unit cell) of the bulk crystal around $\overline{K}$, the D_{6h} symmetry of the crystal is effectively reduced to D_{3h}, allowing a net dipole moment within the *ab*-plane (Fig. 1a). A recent theory has established the general grounds by which such a lack of inversion symmetry of the crystal site point group can lead to a macroscopic spin polarization, driven by the local nature of spin–orbit coupling[6]. Indeed, our calculated bulk wavefunctions projected onto either WSe_2 layer of the unit cell are almost fully spin polarized for the topmost two valence bands at $\overline{K}$ (Fig. 2g). The 180° rotation of neighbouring layers in AB-stacked WSe_2, however, ensures that the sign of the spin polarization is opposite between adjacent layers (Fig. 2h). This leads to a strong spin–layer locking[7,8], with an overall spin degeneracy of the bulk electronic structure as required for a centrosymmetric material. Photoemission, being extremely surface sensitive, can be expected to predominantly probe the top layer of this material. We thus attribute the strong measured spin polarization we observe here to be a direct observation of a layer-localized spin-polarization of bulk electronic states in WSe_2.

This is further supported by our photon-energy-dependent measurements (Fig. 2i), which show how the measured photoelectron spin polarization at $\overline{K}$ can be tuned nearly to zero. Our model calculations (see also Supplementary Fig. 3 and

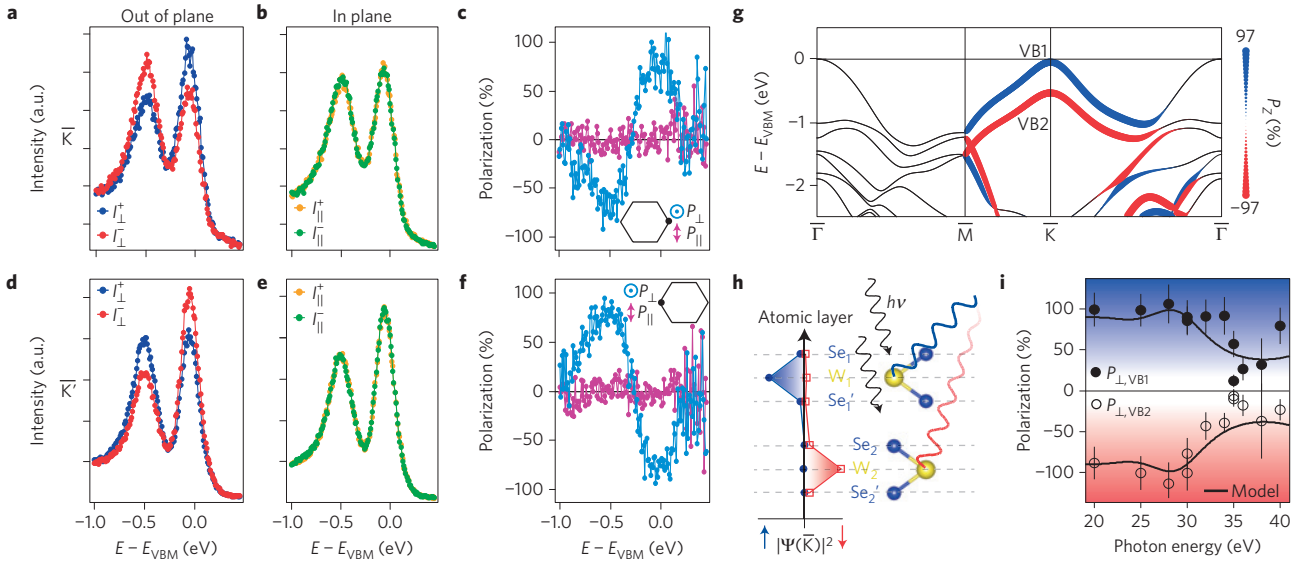

Figure 2 | Observation of spin-polarized bulk bands in an inversion-symmetric host. a,**b**, Energy distribution curves (in arbitrary units (a.u.)) from spin-resolved ARPES measurements ($h\nu = 25$ eV, $T = 300$ K) at the $\overline{K}$ point measured by the out-of-plane ($I_\perp$) (**a**) and in-plane ($I_\parallel$) (**b**) detectors in the Mott scattering chamber (corresponding measurements correcting for the finite Mott-detector efficiencies are shown in Supplementary Fig. 2). **c**, The extracted polarizations show a strong out-of-plane spin polarization, opposite for the two valence band peaks. **d**–**f**, Plots as for **a**–**c**, but for the $\overline{K}'$ point, showing that the signs of all components are reversed. **g**, Our projection of the calculated bulk band structure onto the first layer of the unit cell reveals a strong spin polarization of electronic bands localized on this layer (for example, at $\overline{K}$), whose sign is reversed in the second layer of the unit cell, as shown in **h**. **i**, Measured spin polarization at $\overline{K}$ exhibiting a strong photon energy dependence. Error bars reflect an approximate estimate of the uncertainty in extracting the polarization from the experimental measurements, incorporating statistical errors in peak fitting, systematic errors and uncertainty in sample alignment. Our model calculations (solid line, see Supplementary Information) reveal how the photon energy-dependent modulations of the measured spin polarization result from interference between outgoing photoelectrons originating from the different layers of the crystal.

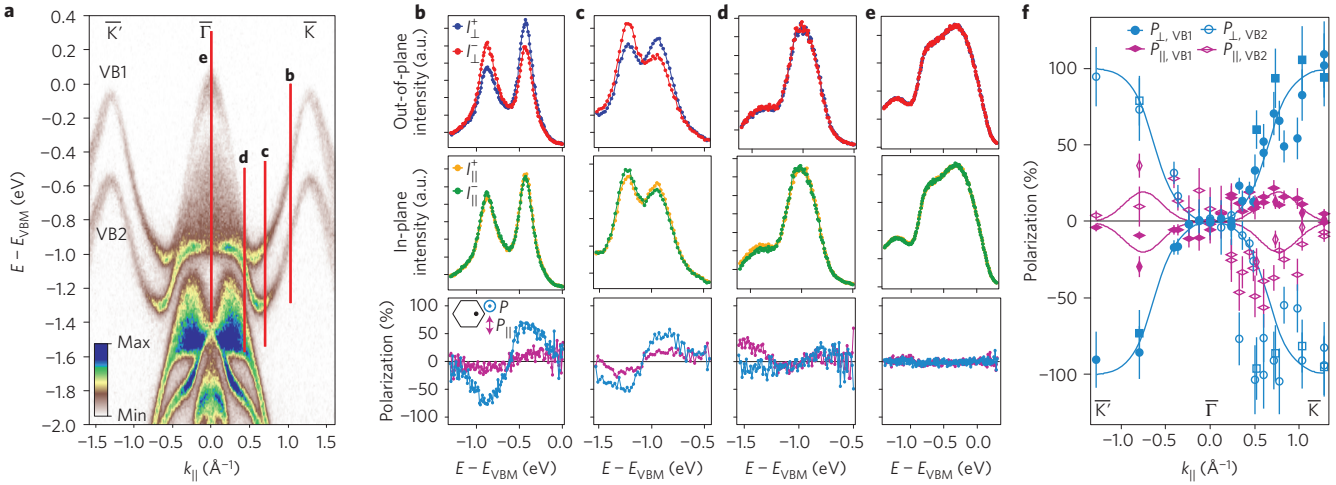

Figure 3 | Evolution of spin texture along $\overline{K}'$–$\overline{\Gamma}$–$\overline{K}$. a, Dispersion measured by ARPES ($h\nu = 125$ eV, $T = 30$ K) along the $\overline{K}'$–$\overline{\Gamma}$–$\overline{K}$ direction. **b**–**e**, Energy distribution curves (EDCs; in arbitrary units (a.u.)) measured using spin-resolved photoemission ($h\nu = 25$ eV, $T = 300$ K) and corresponding extracted spin polarizations, measured at the locations labelled by the corresponding vertical lines in **a**. **f**, The out-of-plane ($P_\perp$) and in-plane ($P_\parallel$) spin polarizations determined from fitting these and additional EDCs ($h\nu = 25$ eV, $T = 80$ K (squares and vertical diamonds, respectively) and $T = 300$ K (circles and horizontal diamonds, respectively)) reveal some canting of the spin into the surface plane away from the $\overline{K}$ points, and a total suppression of the measured spin polarization around the zone centre. Error bars reflect an approximate estimate of the uncertainty in extracting the polarization from the experimental measurements, incorporating statistical errors in peak fitting, systematic errors and uncertainty in sample alignment. The lines in **f** are provided as guides to the eye.

associated discussion) show how this arises as a result of the interference[23,24] of spin-up and spin-down polarized photoelectrons emitted from different layers of the material. This strongly supports our conclusions of a huge momentum-dependent spin splitting of up to ~0.5 eV for bulk states localized in a constituent layer of the unit cell in WSe_2, with a spin orientation that is directly tied to the layer pseudospin. We note that the size of this observed spin splitting greatly exceeds spin–orbit-mediated splittings typically observed so far, even in surface Rashba systems with strong local in-plane field gradients[14,25]. This is because, here, the energy of the spin splitting at the band extrema is directly set by the atomic spin–orbit coupling strength[7].

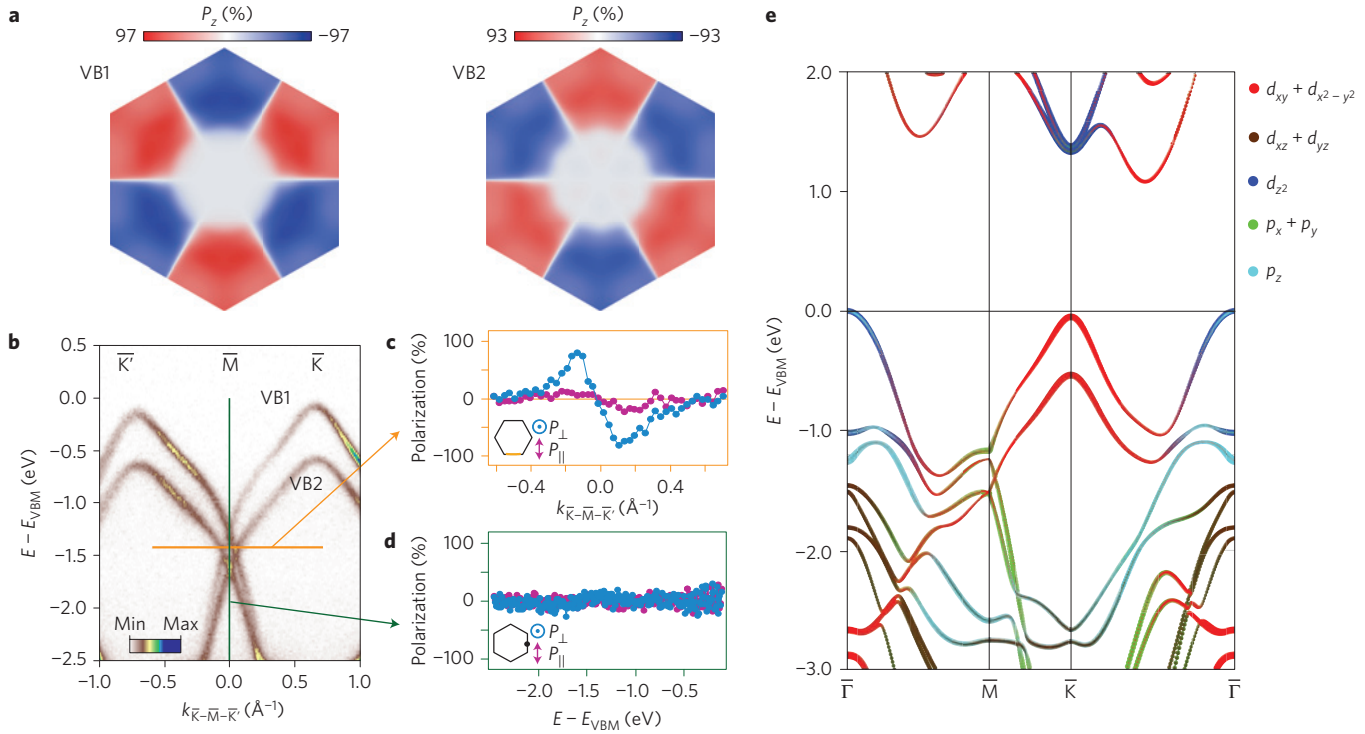

Figure 4 | Momentum-dependent suppression of layer-resolved spin polarization. a, Momentum dependence of the out-of-plane spin polarization of the top two valence bands throughout the Brillouin zone, calculated for the $k_z = 0$ plane and projected onto the first Se–W–Se layer of the unit cell. White regions indicate suppression of the layer-resolved spin-polarization. **b**–**d**, At the $\overline{M}$ point, our ARPES measurements ($h\nu = 125$ eV, $T = 30$ K) (**b**) and corresponding spin polarization determined from spin-ARPES ($h\nu = 25$ eV, $T = 300$ K) along the coloured momentum (**c**) and energy (**d**) distribution curves show how this occurs through the crossing of strongly spin-polarized bands. **e**, In contrast, towards the zone centre, our orbitally projected band structure calculations reveal how this is correlated with the emergence of significant out-of-plane orbital character of the electronic states.

Figure 3 reveals how the underlying spin-polarized states evolve along the $\overline{K}$–$\overline{\Gamma}$–$\overline{K'}$ direction. We find a marked suppression of the out-of-plane spin polarization approximately half way along this line, with negligible polarization observed around the zone centre. This is reproduced by our *ab initio* calculations (Fig. 4a), and can be understood by considering the orbital character of the underlying states (Fig. 4e). Close to $\overline{K}$, the electronic states are derived mostly from d_{xy} and $d_{x^2-y^2}$ orbitals. There is thus significant orbital overlap within the surface plane, which, together with the net in-plane dipole, favours strong out-of-plane spin polarization[26]. Around $\overline{\Gamma}$, however, the orbital character becomes dominantly d_{z^2}/p_z-like, causing this component to be strongly suppressed, as found experimentally, while also driving the observed increase in dimensionality of the electronic states. Intriguingly, we also find a small in-plane spin component emerges along $\overline{K'}$–$\overline{\Gamma}$–$\overline{K}$, which again switches sign either side of $\overline{\Gamma}$. This component would not naively be expected given the symmetry of the Se–W–Se layer, which has no net dipolar field along the out-of-plane direction, as we have confirmed by explicit slab calculations for an ideal bulk-like termination. The emergence of this component therefore reflects further complexity beyond that considered in our theoretical approach, such as small surface relaxations leading to a non-negligible contribution of the dipole out of the surface plane. We stress, however, that this has only a small effect and the predominant contributions to the strong out-of-plane spin polarizations observed here are intrinsic to the bulk electric structure.

We also find a suppression of this out-of-plane spin polarization along the entire $\overline{M}$–$\overline{\Gamma}$ direction. Unlike at the zone centre, however, this cannot be attributed to a change in orbital character: the electronic states close to $\overline{M}$ are predominantly derived from planar orbitals, similar to around $\overline{K}$, and we accordingly find strong layer-resolved spin polarizations of the underlying bands close to $\overline{M}$ (Fig. 4). Rather, the suppression of spin polarization along $\overline{M}$–$\overline{\Gamma}$ is mediated by the degeneracy of two oppositely polarized bands within a single layer. At the $\overline{M}$ point itself, this is a natural consequence of time-reversal symmetry, as $\overline{M}$ is a time-reversal invariant momentum. Along the $\overline{M}$–$\overline{\Gamma}$ line, such degeneracies are enforced by the combination of time-reversal with the rotational D_{3h} symmetry of a single monolayer within the unit cell, ensuring that the out-of-plane component of the spin must have opposite sign in neighbouring sextants of the Brillouin zone.

Together, our calculations and experiment thus point to an extremely rich real- and momentum-space-dependent spin texture of bulk transition-metal dichalcogenides. They provide a direct demonstration of a pronounced coupling between the spin, valley and layer degrees of freedom, of key importance to widespread proposals to use these materials in exotic devices exploiting the valley pseudospin[7,8,19–21,27–29]. More generally, our experimental measurement of spin-polarized bulk electronic states in a centrosymmetric material opens a wealth of new opportunities for creating, probing and controlling spin and valley polarization in bulk solids via local inversion asymmetry.

Methods

ARPES. ARPES measurements were performed at the I05 beamline of Diamond Light Source, UK, and spin-ARPES measurements at the I3 beamline of MAX-III synchrotron, Sweden[30]. Single-crystal samples of WSe_2, grown by the chemical vapour transport method, were cleaved *in situ* and measured at temperatures ranging from 30 to 300 K. Measurements were performed using *p*-polarized synchrotron light from 20 to 130 eV (ARPES) and from 20 to 40 eV (spin-ARPES), and employing Scienta R4000 hemispherical electron analysers.

For the spin-ARPES measurements, a mini-Mott detector scheme was used, permitting simultaneous detection of the out-of-plane and one in-plane (along the analyser slit direction) component of the photoelectron spin[30]. A Sherman function of $S=0.17$ was used to generate the measured spin polarizations[30]

$$P_i = \frac{(I_i^+ - I_i^-)}{S(I_i^+ + I_i^-)}$$

where P_i is the photoelectron spin polarization measured along the out-of-plane, $i=\perp$, or in-plane, $i=\parallel$, direction, and $I_i^{\pm}$ is the measured intensity on the individual detectors in the Mott scattering chamber, corrected by a relative detector efficiency calibration. To extract numerical values of the polarization, we fitted the measured EDCs to two Lorentzian peaks and a Shirley background, convolved with a Gaussian function to account for the instrumental resolution, with the corresponding Lorentzian peak areas used to derive the measured spin polarization. We also applied a geometrical correction to account for the finite angle between the sample and the electron spectrometer, and the corresponding influence of this on the spin polarization measured in the reference frame of the spectrometer. To determine the k_z dispersion from photon-energy-dependent ARPES, we employed a free electron final state model

$$k_z = \sqrt{2m_e/\hbar^2}(V_0 + E_k\cos^2\theta)^{1/2}$$

where θ is the in-plane emission angle and V_0 is the inner potential. Our photon energy range covers more than six complete Brillouin zones along k_z, and we find best agreement taking an inner potential of 13 eV and a c-axis lattice constant of 13.45 Å.

Calculations. Electronic structure calculations were performed within the context of density functional theory (DFT) using the modified Becke–Johnson exchange potential and Perdew–Burke–Ernzerhof correlation functional as implemented in the WIEN2K programme[31]. Relativistic effects, including spin–orbit coupling, were fully included. The Brillouin zone was sampled by a $12\times12\times6$ k-mesh. For the orbital and layer projection calculation, a tight binding Hamiltonian for the bulk band structure was constructed by downfolding the DFT results using maximally localized Wannier functions[32–34], employing W 5d and 5s orbitals and Se 5p and 5s orbitals as a basis.

Received 1 June 2014; accepted 19 August 2014; published online 5 October 2014

References

1. Koo, H. C. *et al.* Control of spin precession in a spin-injected field effect transistor. *Science* **325,** 1515–1518 (2009).
2. Hsieh, D. *et al.* A topological Dirac insulator in a quantum spin Hall phase. *Nature* **452,** 970–974 (2008).
3. Bahramy, M. *et al.* Emergent quantum confinement at topological insulator surfaces. *Nature Commun.* **3,** 1159 (2012).
4. Murakawa, H. *et al.* Detection of Berry's phase in a bulk Rashba semiconductor. *Science* **342,** 1490–1493 (2013).
5. Mourik, V. *et al.* Signatures of Majorana fermions in hybrid superconductor–semiconductor nanowire devices. *Science* **336,** 1003–1007 (2012).
6. Zhang, X., Liu, Q., Luo, J. W., Freeman, A. J. & Zunger, A. Hidden spin polarization in inversion-symmetric bulk crystals. *Nature Phys.* **10,** 387–393 (2014).
7. Gong, Z. *et al.* Magnetoelectric effects and valley-controlled spin quantum gates in transition metal dichalcogenide bilayers. *Nature Commun.* **4,** 2053 (2013).
8. Jones, A. M. *et al.* Spin-layer locking effects in optical orientation of exciton spin in bilayer WSe_2. *Nature Phys.* **10,** 130–134 (2014).
9. Datta, S. & Das, B. Electronic analog of the electro-optic modulator. *Appl. Phys. Lett.* **56,** 665–667 (1990).
10. Das, T. & Balatsky, A. V. Engineering three-dimensional topological insulators in Rashba-type spin–orbit coupled heterostructures. *Nature Commun.* **4,** 1972 (2013).
11. Zhou, J. J., Feng, W., Zhang, Y., Yang, S. A. & Yao, Y. Engineering topological surface states and giant Rashba spin splitting in BiTeI/Bi_2Te_3 heterostructures. *Sci. Rep.* **4,** 3841 (2014).
12. Bychkov, Y. A. & Rashba, E. I. Properties of a 2D electron gas with lifted spectral degeneracy. *JETP Lett.* **39,** 78–81 (1984).
13. Nitta, J., Akazaki, T., Takayanagi, H. & Enoki, T. Gate control of spin–orbit interaction in an inverted $In_{0.53}Ga_{0.47}As/In_{0.52}Al_{0.48}As$ heterostructure. *Phys. Rev. Lett.* **78,** 1335–1338 (1997).
14. Ast, C. R. *et al.* Giant spin splitting through surface alloying. *Phys. Rev. Lett.* **98,** 186807 (2007).
15. King, P. D. C. *et al.* Large tunable Rashba spin splitting of a two-dimensional electron gas in Bi_2Se_3. *Phys. Rev. Lett.* **107,** 096802 (2011).
16. King, P. D. C. *et al.* Quasiparticle dynamics and spin–orbital texture of the $SrTiO_3$ two-dimensional electron gas. *Nature Commun.* **5,** 3414 (2014).
17. Dresselhaus, G. Spin–orbit coupling effects in zinc blende structures. *Phys. Rev.* **100,** 580–586 (1955).
18. Ishizaka, K. *et al.* Giant Rashba-type spin splitting in bulk BiTeI. *Nature Mater.* **10,** 521–526 (2011).
19. Xiao, D., Liu, G-B., Feng, W., Xu, X. & Yao, W. Coupled spin and valley physics in monolayers of MoS_2 and other Group-VI dichalcogenides. *Phys. Rev. Lett.* **108,** 196802 (2012).
20. Mak, K. F., He, K., Shan, J. & Heinz, T. F. Control of valley polarization in monolayer MoS_2 by optical helicity. *Nature Nanotech.* **7,** 494–498 (2012).
21. Zeng, H., Dai, J., Yao, W., Xiao, D. & Cui, X. Valley polarization in MoS_2 monolayers by optical pumping. *Nature Nanotech.* **7,** 490–493 (2012).
22. Finteis, T. *et al.* Occupied and unoccupied electronic band structure of WSe_2. *Phys. Rev. B* **55,** 10400–10411 (1997).
23. Zhu, Z-H. *et al.* Layer-by-layer entangled spin–orbital texture of the topological surface state in Bi_2Se_3. *Phys. Rev. Lett.* **110,** 216401 (2013).
24. Zhu, Z-H. *et al.* Photoelectron spin–polarization control in the topological insulator Bi_2Se_3. *Phys. Rev. Lett.* **112,** 076802 (2014).
25. Bihlmayer, G. *et al.* Enhanced Rashba spin–orbit splitting in Bi/Ag(111) and Pb/Ag(111) surface alloys from first principles. *Phys. Rev. B* **75,** 195414 (2007).
26. Yuan, H. *et al.* Zeeman-type spin splitting controlled by an electric field. *Nature Phys.* **9,** 563–569 (2013).
27. Jones, A. M. *et al.* Optical generation of excitonic valley coherence in monolayer WSe_2. *Nature Nanotech.* **8,** 634–638 (2013).
28. Zhang, Y. J., Oka, T., Suzuki, R., Ye, J. T. & Iwasa, Y. Electrically switchable chiral light-emitting transistor. *Science* **344,** 725–728 (2014).
29. Xu, X., Yao, W., Xiao, D. & Heinz, T. F. Spin and pseudospins in layered transition metal dichalcogenides. *Nature Phys.* **10,** 343–350 (2014).
30. Berntsen, M. H. *et al.* A spin- and angle-resolving photoelectron spectrometer. *Rev. Sci. Instrum.* **81,** 035104 (2010).
31. Blaha, P. *et al.* WIEN2K package, Version 10.1 (2010); http://www.wien2k.at
32. Souza, I. *et al.* Maximally localized Wannier functions for entangled energy bands. *Phys. Rev. B* **65,** 035109 (2001).
33. Mostofi, A. A. *et al.* Wannier90: A tool for obtaining maximally localised Wannier functions. *Comput. Phys. Commun.* **178,** 685–699 (2008).
34. Kuneš, J. *et al.* WIEN2WANNIER: From linearized augmented plane waves to maximally localized Wannier functions. *Comput. Phys. Commun.* **181,** 1888–1895 (2010).

Acknowledgements

We gratefully acknowledge support from the Engineering and Physical Sciences Research Council, UK, the VILLUM foundation, the Calipso program, TRF-SUT Grant RSA5680052 and NANOTEC, Thailand through the CoE Network. P.D.C.K. acknowledges support from the Royal Society through a University Research Fellowship. M.S.B. was supported by a Grant-in-Aid for Scientific Research (S) (No. 24224009) from the Ministry of Education, Culture, Sports, Science and Technology (MEXT) of Japan. The experiments at the MAX IV Laboratory were made possible through funding from the Swedish Research Council and the Knut and Alice Wallenberg Foundation.

Author contributions

J.M.R., F.M., M.D., M.M., L.B., C.G., W.M., J.W.W. and P.D.C.K. measured the experimental data. J.M.R., F.M., J.W.W. and P.D.C.K. analysed the data. M.S.B. performed the electronic structure calculations. T.T. grew the samples. M.L. and T.B. maintained the spin-ARPES end stations and M.H. and T.K.K. maintained the ARPES end stations, respectively, and provided experimental support. P.D.C.K., J.W.W., M.S.B., P.H. and H.T. provided the project infrastructure. All authors discussed the results and their interpretation. P.D.C.K. and J.M.R. wrote the manuscript with input and discussion from all co-authors. P.D.C.K. was responsible for overall project planning and direction.

Additional information

Supplementary information is available in the online version of the paper. Reprints and permissions information is available online at www.nature.com/reprints. Correspondence and requests for materials should be addressed to P.D.C.K.

Competing financial interests

The authors declare no competing financial interests.

เอกสารที่ 3

King P.D.C., Walker S.M., Tamai A., De La Torre A., Eknapakul T., Buaphet P., Mo S.-K., **Meevasana W.**, Bahramy M.S., Baumberger F., Quasiparticle dynamics and spin-orbital texture of the SrTiO3 two-dimensional electron gas, Nature Communications 5, 3414 (2014) (7 citations, 11/6/2015)

nature COMMUNICATIONS

ARTICLE

Received 18 Sep 2013 | Accepted 7 Feb 2014 | Published 27 Feb 2014

DOI: 10.1038/ncomms4414

Quasiparticle dynamics and spin–orbital texture of the $SrTiO_3$ two-dimensional electron gas

P.D.C. King[1,2], S. McKeown Walker[3], A. Tamai[3], A. de la Torre[3], T. Eknapakul[4], P. Buaphet[4], S.-K. Mo[5], W. Meevasana[4], M.S. Bahramy[6,7] & F. Baumberger[2,3,8]

Two-dimensional electron gases (2DEGs) in $SrTiO_3$ have become model systems for engineering emergent behaviour in complex transition metal oxides. Understanding the collective interactions that enable this, however, has thus far proved elusive. Here we demonstrate that angle-resolved photoemission can directly image the quasiparticle dynamics of the *d*-electron subband ladder of this complex-oxide 2DEG. Combined with realistic tight-binding supercell calculations, we uncover how quantum confinement and inversion symmetry breaking collectively tune the delicate interplay of charge, spin, orbital and lattice degrees of freedom in this system. We reveal how they lead to pronounced orbital ordering, mediate an orbitally enhanced Rashba splitting with complex subband-dependent spin–orbital textures and markedly change the character of electron–phonon coupling, co-operatively shaping the low-energy electronic structure of the 2DEG. Our results allow for a unified understanding of spectroscopic and transport measurements across different classes of $SrTiO_3$-based 2DEGs, and yield new microscopic insights on their functional properties.

[1] Kavli Institute at Cornell for Nanoscale Science, Ithaca, New York 14853, USA. [2] SUPA, School of Physics and Astronomy, University of St Andrews, St Andrews, Fife KY16 9SS, UK. [3] Département de Physique de la Matière Condensée, Université de Genève, 24 Quai Ernest-Ansermet, 1211 Genève 4, Switzerland. [4] School of Physics and NANOTEC-SUT Center of Excellence on Advanced Functional Nanomaterials, Suranaree University of Technology, Nakhon Ratchasima 30000, Thailand. [5] Advanced Light Source, Lawrence Berkeley National Lab, Berkeley, California 94720, USA. [6] Quantum-Phase Electronics Center, Department of Applied Physics, The University of Tokyo, Tokyo 113-8656, Japan. [7] RIKEN Center for Emergent Matter Science (CEMS), Wako 351-0198, Japan. [8] Swiss Light Source, Paul Scherrer Institut, CH-5232 Villigen PSI, Switzerland. Correspondence and requests for materials should be addressed to P.D.C.K. (email: philip.king@st-andrews.ac.uk) or to F.B. (email: felix.baumberger@unige.ch).

The ubiquitous perovskite oxide $SrTiO_3$, a wide-gap band insulator, hosts varied bulk properties including quantum paraelectricity, dilute doping-induced superconductivity and high thermoelectric coefficients. These reflect a subtle competition between interactions of the underlying quantum many-body system. Intriguingly, thermodynamic and transport measurements[1–6] indicate that the balance of these interactions can be tuned to engineer striking emergent properties when quantum confinement and doping are combined to create a two-dimensional electron gas (2DEG)[1,2,7]. A diverse and attractive array of properties have been uncovered to date in this system, including gate-tuned superconductivity[3,4,8], its coexistence with ferromagnetism[5,6] and enhanced Seebeck coefficients[9], establishing $SrTiO_3$-based 2DEGs as a model platform for use in future multifunctional electronic devices[1].

They are most commonly realised at a polar interface to another band insulator $LaAlO_3$, creating a narrow conducting channel that resides solely within the $SrTiO_3$ (ref. 10). Similar 2DEGs can also be created by interfacing $SrTiO_3$ to a wide array of other band or Mott insulators including $NdAlO_3$ (ref. 11), $LaTiO_3$ (ref. 12) and $GdTiO_3$ (ref. 13), by chemical doping of electrons into narrow $SrTiO_3$ channels[14,15], analogous to δ-doping of semiconductors such as Si, and by field-effect doping in a transistor-style configuration[8]. Moreover, the recent discovery of a 2DEG formed at the free surface of a bulk $SrTiO_3$ crystal opens new avenues for its advanced spectroscopic investigation[7,16].

Exploiting this, here we present unified angle-resolved photoemission (ARPES) measurements and tight-binding supercell calculations revealing new richness of the electronic structure of this model oxide 2DEG. We show how a pronounced orbital ordering mediates an unconventional spin splitting, giving rise to strongly anisotropic and subband-dependent canted spin–orbital textures. The orbitally enhanced Rashba effect explains the pronounced spin splittings previously inferred from magneto-transport in this system, while simultaneously revealing a breakdown of the conventional picture used to describe these. We uncover how this complex ladder of subband states are further renormalized by many-body interactions. This reconciles previous discrepancies between effective masses estimated from ARPES and quantum oscillations, unifying the properties of surface and interface $SrTiO_3$ 2DEGs, and reveals a strikingly different nature of electron–phonon coupling compared with bulk $SrTiO_3$.

Results

Orbital ordering. Figure 1 summarizes the generic electronic structure of $SrTiO_3$ 2DEGs, as revealed by ARPES from a $SrTiO_3$(100) surface with saturated band bending[7]. Consistent with previous reports from both surface and interface 2DEGs[7,16–19], we find a broad bandwidth that extends up to $\approx$250 meV below the Fermi level. Here we can resolve a ladder of at least three light subband states that contribute concentric circular Fermi surface sheets, co-existing with just a single heavy electron band ($m^* = 14 \pm 3m_e$) that has a much shallower binding energy of $<$50 meV and gives rise to elliptical Fermi surfaces oriented along $\langle 10 \rangle$. From this Fermi surface topology together with the polarization dependence of our measured intensities (Supplementary Fig. 2), we assign not only the lowest[16] but rather the whole ladder of observed light states as having dominantly d_{xy} orbital character, while the heavy states derive from $d_{xz/yz}$ orbitals. This immediately indicates a strong breaking of the t_{2g} orbital degeneracy that is present in the bulk electronic structure of $SrTiO_3$ (ref. 20), driving a pronounced orbital ordering with a polarization $P = \frac{n(d_{xy}) - n(d_{xy/yz})}{n(d_{xy}) + n(d_{xy/yz})}$, which exceeds 30%, a lower limit derived from our experimentally resolved Fermi surface areas.

This is a direct consequence of the real-space anisotropy of the orbital wavefunctions combined with inversion symmetry breaking by the electrostatic potential that defines the 2DEG by creating a steep asymmetric quantum well along the z direction (Fig. 1c). As shown by our self-consistent tight-binding supercell calculations (Fig. 1b, see Methods), the resulting quantized subbands that derive from planar d_{xy} orbitals have wavefunctions reminiscent of the envelope functions of a semiconductor quantum well, except that in $SrTiO_3$ they are much more localized in real space, almost to within a single unit cell for the lowest subband state. In contrast, the potential variation acts as a

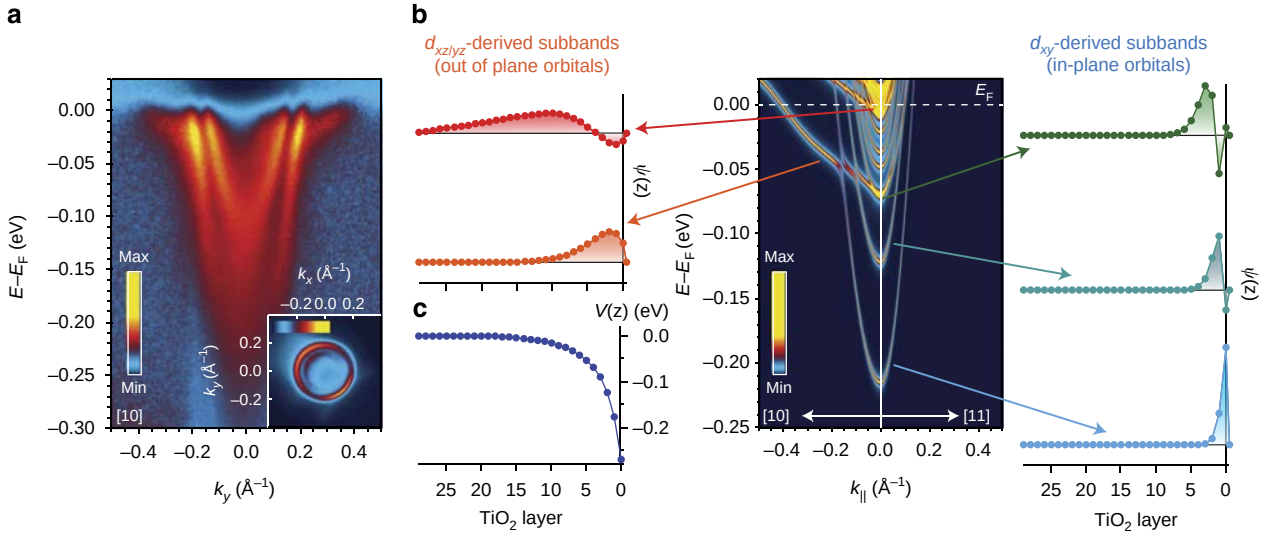

Figure 1 | Orbital ordering of a 2D electron gas in $SrTiO_3$. (**a**) E versus k dispersion from ARPES ($h\nu = 50$ eV, measured along the [10] direction), revealing a multi-orbital subband structure comprising co-existing ladders of light and massive d-electron subband states. The respective circular and faint elliptical Fermi surface pockets (measured with $h\nu = 51$ eV and the polarization along [11]) are shown in the inset. For the dispersion plot, a normalization (division by the average MDC) has been applied to better reveal the massive band, as shown in Supplementary Fig. 1. (**b**) This electronic structure is well described by a self-consistent tight-binding supercell calculation. The spatial dependence of the subband wavefunctions along the confinement direction, $\Psi(z)$, reveal a pronounced real-space orbital ordering, a direct consequence of near-surface band bending (**c**).

much weaker perturbation on the out-of-plane $d_{xz/yz}$ orbitals, which have much larger hopping amplitudes along the z direction. The resulting subbands sit close to the top of the potential well, leading to wavefunctions that penetrate much deeper into the bulk. This disparate spatial extent of the subband states is consistent with their relative spectral weight in our surface-sensitive ARPES measurements.

Unconventional Rashba spin splitting. The same breaking of inversion symmetry that drives this orbital ordering can additionally lift the spin degeneracy through a Bychkov–Rashba-type spin–orbit interaction[21–23]. Focussing near the band bottom of the lowest d_{xy} band (Fig. 2a,b), we indeed find a small characteristic splitting between the calculated energy of spin-up and spin-down states, $\delta E = 2\alpha k_{||}$, with a Rashba parameter, $\alpha = 0.003$ eVÅ. The non-negligible splitting found here, despite the modest spin–orbit interaction in $3d$ transition metals, is indicative of the very strong electric field gradient of the confining potential. From our self-consistent band-bending potential calculation (Fig. 1c), we estimate that this exceeds 2×10^8 V m^{-1} within the first two unit cells where the lowest subband state is confined. For the more delocalized second d_{xy} subband, whose wavefunction extends into regions of shallower band bending, we find a slightly smaller Rashba parameter $\alpha = 0.0014$ eVÅ, confirming that the strength of this spin splitting is controlled by the confining electric field. This should therefore be directly tuneable by electrical gating, suggesting a potential route towards spintronic control in oxides.

Unlike typical Rashba systems such as the Au(111) surface, however, here the interplay between orbital ordering and spin–orbit coupling leads to a significantly richer spin structure of the 2DEG states. Close to the crossings of the light d_{xy} and heavy $d_{xz/yz}$ subbands, the spin splitting increases by approximately an order of magnitude, concomitant with a strong mixing of their orbital character (Fig. 2a–c). This rationalizes an increased spin splitting reported from transport when the $d_{xz/yz}$ subbands become populated in electrically gated $SrTiO_3/LaAlO_3$ interface 2DEGs[24]. Moreover, the crossover from k-linear to strongly enhanced spin splitting that we find here readily explains the approximately k^3 dependence of the splitting that has been reported[25]. Our layer-projected calculations indicate that the subband wavefunctions become more delocalized in the z direction close to these band crossings, a natural consequence of the stronger overlap of neighbouring $d_{xz/yz}$ orbitals along z (Supplementary Fig. 3). This delocalization would naively be expected to reduce the strength of the Rashba effect. In contrast, its significant enhancement here points to a dominant role of inter-orbital hopping in driving such surprisingly large spin splittings. Similar enhancements have recently also been observed in other calculations, mainly based on model 3-band Hamiltonians[26–28], which are qualitatively entirely consistent with our results. Our calculations demonstrate how this is a direct consequence of orbital ordering in the

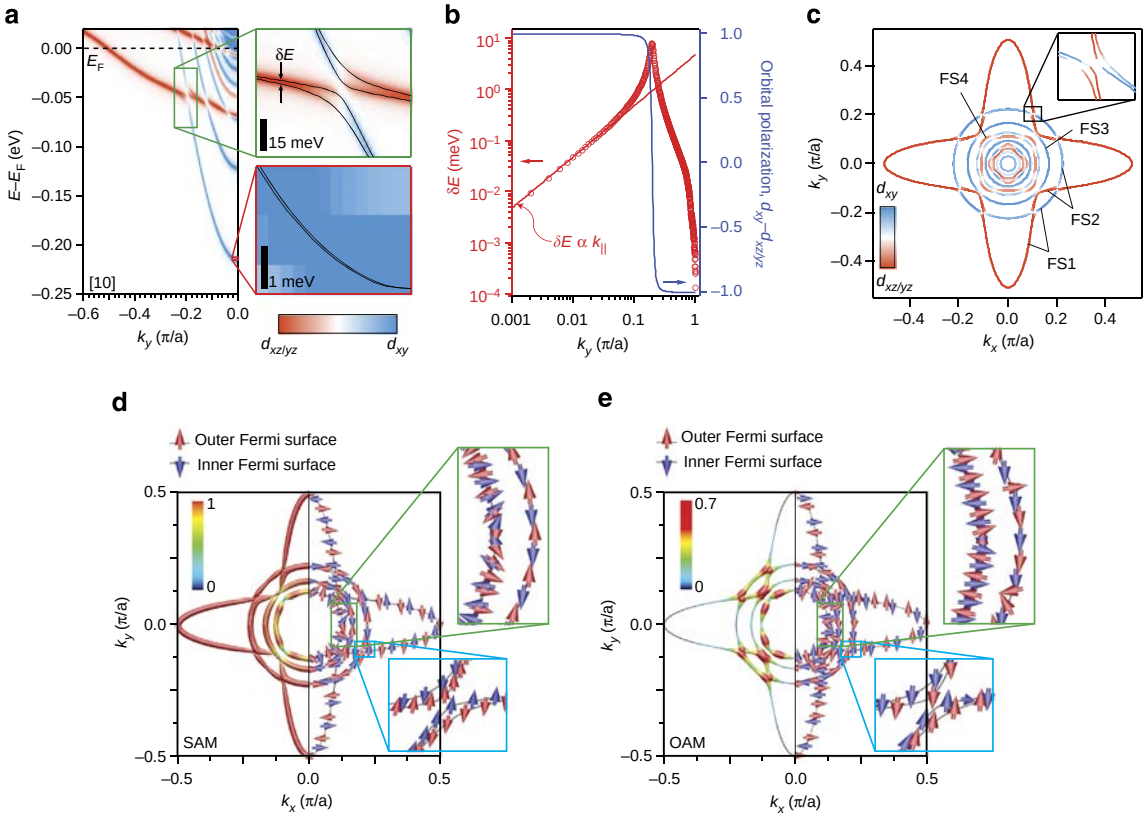

Figure 2 | Orbitally enhanced spin splitting. (**a**) Orbitally resolved electronic structure of the 2DEG along the [10] direction. Magnified views reveal a weak Rashba-type spin splitting around the band bottom, which becomes enhanced by approximately an order of magnitude at the crossings of the light and heavy subband states where the orbital character becomes strongly mixed, as quantified in (**b**) for the lowest subbands. (**c**) The calculated Fermi surface shows how similar orbital mixing and pronounced spin splittings occur at the crossings of circular d_{xy}- and elliptical $d_{xz/yz}$-derived Fermi surface sheets. This gives rise to an exotic anisotropic and subband-specific coupled spin–orbital texture of the 2DEG, as evident from the magnitude (left) and direction (right) of the (**d**) spin, SAM and (**e**) orbital, OAM, angular momenta of the four largest Fermi surface sheets. The magnitude of the SAM (OAM) is represented on a false colour scale in units of $\hbar/2$ ($\hbar$), respectively, and is shown for additional Fermi surfaces in Supplementary Fig. 4.

real experimentally confirmed multi-subband structure of the $SrTiO_3$ 2DEG.

Moreover, as shown in Fig. 2d,e, they reveal an exotic coupled spin–orbital texture of the resulting 2DEG Fermi surfaces. While an approximately perpendicular spin-momentum locking ensures tangential spin winding around the circular d_{xy} sections of Fermi surface, it leads to spins aligned almost perpendicular to the Fermi surface for large sections of the extremely anisotropic d_{xz} (d_{yz}) sheets. Around the crossings of d_{xy} and $d_{xz/yz}$ states, the spins of neighbouring Fermi surfaces align (anti-)parallel with a $|\downarrow\rangle|\uparrow\rangle|\uparrow\rangle|\downarrow\rangle$ ordering, ensuring maximal hybridization gaps are opened. At the same time, rather than being quenched to zero as might have naively been expected, we find a finite orbital angular momentum (OAM, **L**) emerges. This is relatively small ($\lesssim 0.05\hbar$) for the isolated d_{xy} and $d_{xz/yz}$ sections of Fermi surface (Fig. 2e and Supplementary Fig. 3), but grows as large as $0.7\hbar$ around the band crossings. Moreover, we find that the OAM is oriented either parallel or antiparallel to the corresponding spin angular momentum (SAM, **S**), and so this increase in OAM maximally enhances $\mathbf{L}\cdot\mathbf{S}$, by a factor of ~ 14, at and in the vicinity of the hybridization gaps, comparable to the corresponding increase in spin splitting (Fig. 2b).

This therefore provides a natural basis to understand the large spin splittings inferred from magnetotransport[29–31], despite the small atomic spin–orbit interaction of $SrTiO_3$, in terms of an orbital Rashba effect[32,33]. For isolated d_{xy} sections of Fermi surface, we find that the OAM of the inner and outer spin-split branches have the same helicity, consistent with a weak spin–orbit coupling limit[33]. For the $d_{xz/yz}$ sections of Fermi surface, however, the inner and outer branches have opposite OAM, reflecting additional richness as compared with model systems such as noble metal surface states[33]. This causes mixed helicities of the OAM around the inner branch of each Fermi surface sheet, as compared with a complete 2π winding for the outer branches (see arrows in Supplementary Fig. 4). Importantly, we find that the dominant inter-band interactions cause the winding direction of both the OAM and SAM of the outer d_{xy}-derived Fermi surfaces to abruptly switch sign across the hybridization gaps. For several inner Fermi surfaces whose orbital character is strongly mixed, continuously evolving between d_{xy}- and $d_{xz/yz}$-like around the Fermi surface (Fig. 2c), this leads to strongly frustrated spin and orbital textures, rapidly canting from tangential to radial alignment as a function of Fermi surface angle (Fig. 2d,e). This is quite distinct from the functional form of conventional Rashba splitting[21] and provides strong constraints for the influence of spin splitting on magnetism[34] and superconductivity[35].

Many-body interactions. In Fig. 3, we further uncover a pronounced role of electron–phonon interactions on this complex hierarchy of electronic states. Unlike in bulk-doped $SrTiO_3$, where the Fermi energy is typically only a few meV and the electron–phonon interaction is thus non-retarded, the occupied widths of different subbands of the 2DEG range from almost zero up to values greater than the highest phonon frequency of ≈ 100 meV. This is an unusual situation, neither described by the adiabatic ($\hbar\omega_D << E_F$) nor the anti-adiabatic ($\hbar\omega_D >> E_F$) approximation, and points to a complex influence of electron–phonon coupling in this system. We extract the corresponding self-energy, $\Sigma_{e-ph}(\omega) = \Sigma'(\omega) + i\Sigma''(\omega)$, from our ARPES measurements of the lowest subband along the [11] direction (see methods), where we resolve an isolated band all the way up to E_F. The slope of Σ' at the Fermi level yields an electron–phonon coupling strength of $\lambda = 0.7(1)$, while its broad maximum between $\approx 20-60$ meV is indicative of coupling to multiple modes. Indeed, the experimentally determined self-energy is in excellent agreement with a calculation within Eliashberg theory that assumes a coupling function $\alpha^2F(\omega)$ proportional to the entire phonon density of states associated with the motion of oxygen and Ti ions[36] and includes the realistic 2DEG electron density of states from our tight-binding calculation.

Together with a moderate correlation-induced mass enhancement of ≈ 1.4 that we estimate from a Kramers–Kronig transform of a Fermi-liquid contribution to the imaginary part

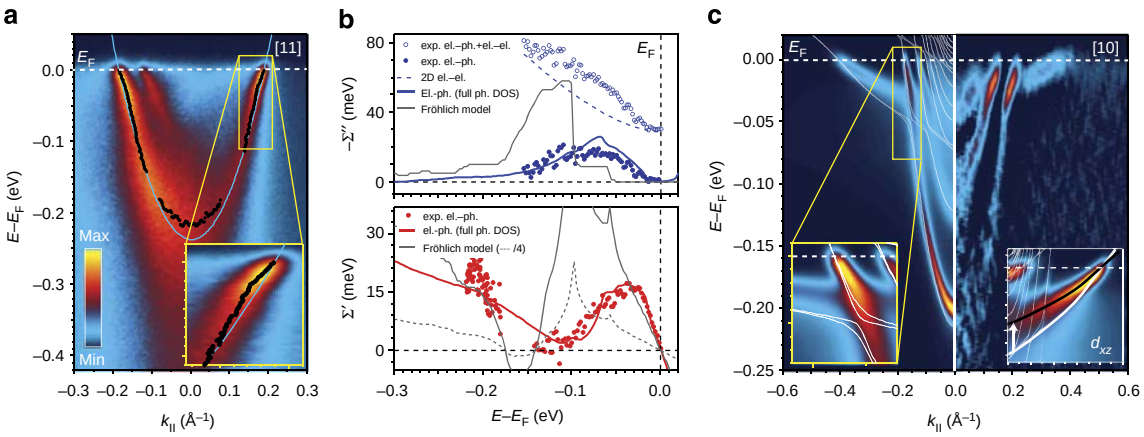

Figure 3 | Quasiparticle dynamics of the subband states. (**a**) ARPES measurements along the [11] direction ($h\nu = 51$ eV), together with the peak positions of fits to MDCs and EDCs (black dots) and a cosine 'bare band' dispersion (blue line). The data reveal pronounced signatures of electron–phonon coupling. Particularly apparent is a low-energy kink in the dispersion at $\omega \approx 30$ meV, shown magnified inset. (**b**) Real, Σ', and imaginary, Σ'', parts of the extracted self-energy. The open blue symbols show Σ'' before subtraction of an electron–electron scattering contribution to the total measured imaginary part of the self-energy, approximated here by the expression $\Sigma''_{e-e}(\omega) = \beta\omega^2(1 + 0.53\ln(\omega/E_F))$ for a 2D Fermi liquid (dashed line, $\beta = 1.5\,\mathrm{eV}^{-1}$, $E_F = 0.25$ eV). The solid lines are calculated electron–phonon self energies with the Eliashberg function proportional to the full phonon density of states (red/blue) or for coupling to three LO phonons (black), which dominate the interaction in lightly doped bulk $SrTiO_3$. (**c**, left) Calculated electron–phonon spectral function, $A(k,\omega)$, along the [10] direction (see Methods). This reveals complete bandwidth renormalization of the heavy states (particularly apparent when $A(k,\omega)$ is projected only onto d_{xz} orbitals as shown in the right inset), and kinks in the light d_{xy} subband dispersions at their crossings with this renormalized heavy state (left inset), both in good agreement with our experimental measurements, shown in the right half using curvature analysis[46] of the raw data.

of the self-energy, our analysis suggests an overall mass enhancement arising from many-body interactions of $m^*/m_{band} \approx 2.1$, close to the values deduced for lightly doped bulk $SrTiO_3$ from measurements of the electronic specific heat[37] and optical spectroscopy[38]. The nature of the electron–phonon coupling, however, is very different. In lightly doped bulk $SrTiO_3$, it is dominated by long-range coupling to longitudinal optical (LO) phonons as described by the Fröhlich model[38,39]. This model predicts much weaker coupling to low-energy modes than observed here, but a significantly stronger coupling to the highest LO phonon at 100 meV, as evident from a calculation employing coupling strengths from bulk $SrTiO_3$ (refs 39,40), which yield an electron–phonon self-energy in clear contrast to our experimental findings (Fig. 3b).

The electric field that confines the 2DEG is known to dramatically reduce its dielectric constant[7,41]. This, together with higher carrier densities as compared with bulk $SrTiO_3$, will lead to shorter electronic screening lengths for the 2DEG, explaining the observed suppression of long-range coupling to LO modes. The enhanced coupling to low-energy phonons for the 2DEG instead leads to a pronounced kink in the dispersion of the d_{xy} subbands at an energy around 30 meV. We resolve these along both the [10] and [11] directions for the first two d_{xy} subbands. Crucially, the resulting enhanced quasiparticle mass, which we estimate as 1.1(2) m_e from our measured Fermi velocities, rectifies the discrepancy between the light masses around 0.6 m_e reported in earlier ARPES studies of $SrTiO_3$ surface 2DEGs[7,16] and recent quantum oscillation experiments that revealed effective masses typically around 1m_e (refs 42,43).

Intriguingly, along [10] the kink energy coincides almost exactly with the crossing of the light d_{xy} and heavy d_{xz} subband states. This behaviour is well captured by our spectral function simulations calculated from our tight-binding bare dispersions and electron–phonon self-energy. These illustrate a very different effect of electron–phonon interactions on the heavy compared with the light subbands of the 2DEG, the former coupling to phonons with frequencies ranging from below to above the bare bandwidth. Our calculations reveal that electron–phonon coupling essentially results in an overall bandwidth renormalization of these states, in agreement with our experimental data where we find the band bottom of the heavy state substantially above the value predicted by our model tight-binding calculations.

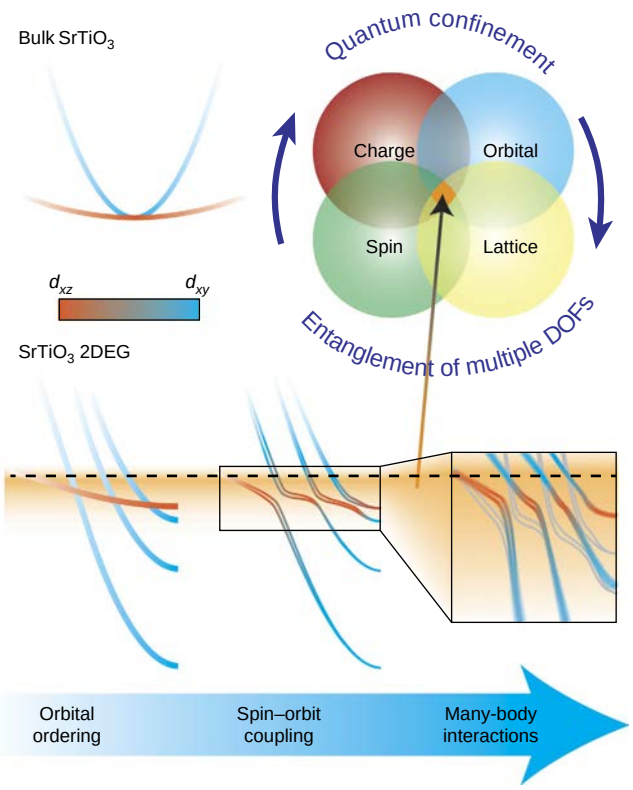

Figure 4 | Hierarchy and interplay of underlying degrees of freedom. In the formation of the 2DEG, quantum confinement reconstructs the bulk electronic structure into a rich array of intersecting orbitally ordered subband states. The interplay of this with spin–orbit coupling lifts the spin degeneracy of these bands, particularly strong around their crossings, through an orbitally enhanced Rashba-like interaction. Electron–phonon and electron–electron interactions further renormalise these spin-split dispersions, increasing the quasiparticle masses close to the Fermi level and causing a complete bandwidth narrowing of the shallow $d_{xz/yz}$ states that pins the orbitally ordered band crossings close to the energy of the lowest phonon mode. This, in turn, sets the energy scale for enhanced spin–orbit splittings around these crossings, strongly entangling the charge, spin, orbital and lattice degrees of freedom of the 2DEG on a low-energy scale (orange shading).

Discussion

The combination of electron–phonon coupling with orbital ordering therefore effectively pins the crossings of the d_{xy} and $d_{xz/yz}$ subbands to the low-energy peak in the phonon density of states. As demonstrated above, however, we additionally find orbitally enhanced spin–orbit splittings that become maximal around these band crossings. Our direct spectroscopic measurements, together with our theoretical calculations, therefore demonstrate how a co-operative effect of orbital ordering and electron–phonon coupling sets the relevant energy scale for dominant spin splitting in this system.

Together, this reveals an intricate hierarchy of interactions and orderings governing the low-energy electronic structure of the $SrTiO_3$ 2DEG (Fig. 4). Electrostatic screening in response to a surface or interface charge generates an electron accumulation layer confined to a narrow potential well. The resulting quantum size effects drive pronounced orbital ordering, creating multiple intersections of light d_{xy}- and heavy $d_{xz/yz}$-derived subband states. This leads to orbital mixing and induces a significant local orbital angular momentum, which in turn permits a pronounced spin splitting to emerge, despite modest atomic spin–orbit coupling. Many-body interactions, of strikingly different form to the bulk, enhance the quasiparticle masses of these spin-split subbands, reduce their bandwidths and renormalize the energetic locations of their intersections, thus modulating their unconventional spin splitting.

Together, this interplay strongly entangles the charge, spin, orbital and lattice degrees of freedom of the $SrTiO_3$ 2DEG on an energy scale $\lesssim$30 meV. This will dominate both its transport and thermodynamic properties. Already we have shown how this explains enhanced quasiparticle masses observed from quantum oscillations as well as signatures of spin splitting in magnetotransport, unifying electrical and spectroscopic measurements from surface- and interface-based $SrTiO_3$ 2DEGs. More generally, it establishes how quantum size effects can dramatically manipulate the underlying electronic landscape of interacting electron liquids, setting the stage for engineering new emergent properties by dimensional confinement in transition metal oxides.

Methods

Angle-resolved photoemission. ARPES measurements were performed at the CASIOPEE beamline of SOLEIL synchrotron, the SIS beamline of the Swiss Light Source, and beamline 10.0.1 of the Advanced light source using Scienta R4000

hemispherical electron analysers, and with base pressures $<5\times10^{-11}$ mbar. Single crystal $SrTiO_3$ commercial wafers were cleaved *in situ* at the measurement temperature of $T=20$–30 K along notches defining a (100) plane. Measurements were performed on stoichiometric transparent insulating samples as well as very lightly La-doped samples ($Sr_{1-x}La_xTiO_3$ with $x=0.001$) to help avoid charging. 2DEGs were induced at the bare surface by exposure to intense UV synchrotron light[7]. The samples were exposed to irradiation doses $\gtrsim1{,}000\,J\,cm^{-2}$ to saturate the formation of the 2DEG, and we experimentally confirmed that saturation was reached before starting any of the measurements presented here. The data shown here was measured using *s*-polarized photons of 51 or 55 eV, except for the Fermi surface maps shown in Supplementary Fig. 2 that used 43-eV *s*- and *p*-polarized light. All measurements were performed in the second Brillouin zone.

Self-energy determination. To determine the electron–phonon self-energy experimentally, we fit momentum distribution curves (MDCs) and energy distribution curves (EDCs) of the lowest d_{xy} subband measured along the [11] direction. We chose this band as its dispersion does not intersect that of the heavy $d_{xz/yz}$ subbands up to the chemical potential along this direction (Fig. 1b), allowing us to perform a quantitative analysis over an extended energy range, free from complications associated with the hybridization of different subbands. The real part of the self-energy, $\Sigma'(\omega)$, is given by the difference between our extracted dispersion and that of a 'bare' band. In order to derive a Kramers–Kronig consistent self-energy, we take the cosine bare band shown in Fig. 3a, which includes a moderate bandwidth renormalization due to electron correlations. We extract the imaginary part of the self-energy, $\Sigma''(\omega)=\Delta k(\omega)/2\cdot\partial\epsilon/\partial k$, where Δk is the full width at half maximum of Lorentzian fits to MDCs, and $\partial\epsilon/\partial k$ is the bare band dispersion. This results in an imaginary part that includes a contribution from electron–electron interactions, which we approximate by the expression for a two-dimensional Fermi liquid $\Sigma''_{e-e}(\omega)=\beta\omega^2(1+0.53\ln(\omega/E_F))$. Subtracting this contribution with realistic parameter values of $\beta=1.5\,eV^{-1}$ and $E_F=0.25$ eV from our total extracted Σ'' (see Fig. 3b) yields the imaginary part of the electron–phonon self-energy.

Electronic structure and self-energy calculations. To calculate the subband structure, we start from a relativistic density functional theory calculation of bulk $SrTiO_3$ using the modified Becke–Johnson exchange potential and Perdew–Burke–Ernzerhof correlation functional as implemented in the WIEN2K programme[44]. The muffin-tin radius of each atom R_{MT} was chosen such that its product with the maximum modulus of reciprocal vectors K_{max} become $R_{MT}K_{max}=7.0$. The Brillouin zone was sampled by a $15\times15\times15$ *k*-mesh. We downfold this using maximally localized Wannier functions to generate a set of bulk tight-binding transfer integrals, and then incorporate these into a 30-unit cell supercell with additional on-site potential terms to account for band bending via an electrostatic potential variation. We solve this self-consistently with Poisson's equation, incorporating an electric field-dependent dielectric constant[41], to yield the bare band dispersions including Rashba-type spin splitting[45] of the 2DEG. We stress that the total magnitude of the band bending is the only adjustable parameter, and yields a realistic electronic structure in good agreement with our spectroscopic measurements apart from our observed signatures of electron–phonon interactions that are not included at the level of density functional theory. To incorporate these, we calculate the self-energy $\Sigma_{e-ph}(\omega)$ in an Eliashberg model,

$$\Sigma_{e-ph}(\omega)=\int_{-E_F}^{\infty}N(\epsilon)d\epsilon\int_0^{\tilde{\omega}_{max}}d\tilde{\omega}\alpha^2F(\tilde{\omega})\times\left\{\frac{f(-\epsilon,T)+n(\tilde{\omega},T)}{\omega-\epsilon-\tilde{\omega}+i\delta^{\pm}}+\frac{f(\epsilon,T)+n(\tilde{\omega},T)}{\omega-\epsilon+\tilde{\omega}+i\delta^{\pm}}\right\}$$

where $N(\epsilon)$ is the bare electronic density of states determined from our tight-binding calculations and $f(\epsilon,T)$ and $n(\tilde{\omega},T)$ are the Fermi and Bose occupation factors. For the coupling function $\alpha^2F(\tilde{\omega})$ we use two different models. The blue line in Fig. 3b assumes $\alpha^2F(\tilde{\omega})$ proportional to the entire O- and Ti-derived phonon density of states from ref. 36, while the black line is a calculation for the coupling strengths given in refs 39,40 for the three LO phonons that were found to dominate the electron–phonon interaction in lightly doped bulk samples. We then calculated the spectral function

$$A(k,\omega)=-\frac{1}{\pi}\frac{\Sigma''(\omega)}{[\omega-\epsilon(k)-\Sigma'(\omega)]^2+[\Sigma''(\omega)]^2}$$

where the bare band dispersion $\epsilon(k)$ is taken from our tight-binding calculation. To better compare with our experimental data in Fig. 3c, we project this onto different atomic orbitals, and include contributions from d_{xy} and d_{xz} but not d_{yz} orbitals to account for transition matrix elements in our experimental geometry. We additionally project the calculation onto different layers of our supercell, and incorporate an exponential attenuation of signal with depth below the surface in photoemission, assuming an inelastic mean free path of 5 Å, into our simulation. Finally, we convolve the simulated spectral function with a 2D Gaussian to account for an experimental energy and momentum resolution of 0.01 eV and $0.015\,Å^{-1}$, respectively.

References

1. Mannhart, J. & Schlom, D. G. Oxide Interfaces–An Opportunity for Electronics. *Science* **327,** 1607–1611 (2010).
2. Hwang, H. Y. *et al.* Emergent phenomena at oxide interfaces. *Nat. Mater.* **11,** 103–113 (2012).
3. Reyren, N. *et al.* Superconducting Interfaces Between Insulating Oxides. *Science* **317,** 1196–1199 (2007).
4. Caviglia, A. D. *et al.* Electric field control of the $LaAlO_3/SrTiO_3$ interface ground state. *Nature* **456,** 624–627 (2008).
5. Bert, J. A. *et al.* Direct imaging of the coexistence of ferromagnetism and superconductivity at the $LaAlO_3/SrTiO_3$ interface. *Nat. Phys.* **7,** 767–771 (2011).
6. Li, L., Richter, C., Mannhart, J. & Ashoori, R. C. Coexistence of magnetic order and two-dimensional superconductivity at $LaAlO_3/SrTiO_3$ interfaces. *Nat. Phys.* **7,** 762–766 (2011).
7. Meevasana, W. *et al.* Creation and control of a two-dimensional electron liquid at the bare $SrTiO_3$ surface. *Nat. Mater.* **10,** 114–118 (2011).
8. Ueno, K. *et al.* Electric-field-induced superconductivity in an insulator. *Nat. Mater.* **7,** 855–858 (2008).
9. Ohta, H. *et al.* Giant thermoelectric Seebeck coefficient of a two-dimensional electron gas in $SrTiO_3$. *Nat. Mater.* **6,** 129–134 (2007).
10. Ohtomo, A. & Hwang, H. Y. A high-mobility electron gas at the $LaAlO_3/SrTiO_3$ heterointerface. *Nature* **427,** 423–426 (2004).
11. Annadi, A. *et al.* Electronic correlation and strain effects at the interfaces between polar and nonpolar complex oxides. *Phys. Rev. B* **86,** 085450 (2012).
12. Ohtomo, A. *et al.* Artificial charge modulation in atomic scale perovskite titanate superlattices. *Nature* **419,** 378–380 (2002).
13. Moetakef, P. *et al.* Electrostatic carrier doping of $GdTiO_3/SrTiO_3$ interfaces. *Appl. Phys. Lett.* **99,** 232116 (2011).
14. Kozuka, Y. *et al.* Two-dimensional normal-state quantum oscillations in a superconducting heterostructure. *Nature* **462,** 487–490 (2009).
15. Choi, W. S., Lee, S., Cooper, V. R. & Lee, H. N. Fractionally δ-doped oxide superlattices for higher carrier mobilities. *Nano Lett.* **12,** 4590–4594 (2012).
16. Santander-Syro, A. F. *et al.* Two-dimensional electron gas with universal subbands at the surface of $SrTiO_3$. *Nature* **469,** 189–193 (2011).
17. D'Angelo, M. *et al.* Hydrogen-induced surface metallization of $SrTiO_3(001)$. *Phys. Rev. Lett.* **108,** 116802 (2012).
18. Berner, G. *et al.* Direct *k*-space mapping of the electronic structure in an oxide-oxide interface. *Phys. Rev. Lett.* **110,** 247601 (2013).
19. Plumb, N. C. *et al.* Mixed dimensionality of confined conducting electrons tied to ferroelectric surface distortion on an oxide. Preprint at http://arxiv.org/abs/arXiv:1302.0708 (2013).
20. Salluzzo, M. *et al.* Orbital reconstruction and the two-dimensional electron gas at the $LaAlO_3/SrTiO_3$ interface. *Phys. Rev. Lett.* **102,** 166804 (2009).
21. Bychkov, Y. A. & Rashba, E. I. Properties of a 2D electron gas with lifted spectral degeneracy. *JETP Lett.* **39,** 78–81 (1984).
22. Grundler, D. Large Rashba splitting in InAs quantum wells due to electron wave function penetration into the barrier layers. *Phys. Rev. Lett.* **84,** 6074–6077 (2000).
23. King, P. D. C. *et al.* Large Tunable Rashba Spin Splitting of a Two-Dimensional Electron Gas in Bi_2Se_3. *Phys. Rev. Lett.* **107,** 096802 (2011).
24. Fête, A., Gariglio, S., Caviglia, A. D., Triscone, J.-M. & Gabay, M. Rashba induced magnetoconductance oscillations in the $LaAlO_3$-$SrTiO_3$ heterostructure. *Phys. Rev. B* **86,** 201105 (2012).
25. Nakamura, H., Koga, T. & Kimura, T. Experimental evidence of cubic Rashba effect in an inversion-symmetric oxide. *Phys. Rev. Lett.* **108,** 206601 (2012).
26. Zhong, Z., Tóth, A. & Held, K. Theory of spin-orbit coupling at $LaAlO_3/SrTiO_3$ interfaces and $SrTiO_3$ surfaces. *Phys. Rev. B* **87,** 161102 (2013).
27. Khalsa, G., Lee, B. & MacDonald, A. H. Theory of t_{2g} electron-gas Rashba interactions. *Phys. Rev. B* **88,** 041302R (2013).
28. Kim, Y., Lutchyn, R. M. & Nayak, C. Origin and transport signatures of spin-orbit interactions in one- and two-dimensional $SrTiO_3$-based heterostructures. *Phys. Rev. B* **87,** 245121 (2013).
29. Caviglia, A. D. *et al.* Tunable Rashba spin-orbit interaction at oxide interfaces. *Phys. Rev. Lett.* **104,** 126803 (2010).
30. Ben Shalom, M., Sachs, M., Rakhmilevitch, D., Palevski, A. & Dagan, Y. Tuning spin-orbit coupling and superconductivity at the $SrTiO_3/LaAlO_3$ interface: a magnetotransport study. *Phys. Rev. Lett.* **104,** 126802 (2010).
31. Joshua, A., Pecker, S., Ruhman, J., Altman, E. & Ilani, S. A universal critical density underlying the physics of electrons at the $LaAlO_3/SrTiO_3$ interface. *Nat. Commun.* **3,** 1129 (2012).
32. Park, S. R. *et al.* Orbital-angular-momentum based origin of Rashba-type surface band splitting. *Phys. Rev. Lett.* **107,** 156803 (2011).
33. Kim, B. *et al.* Spin and orbital angular momentum structure of Cu(111) and Au(111) surface states. *Phys. Rev. B* **85,** 195402 (2011).
34. Fischer, M. H., Raghu, S. & Kim, E.-A. Spin-orbit coupling in $LaAlO_3/SrTiO_3$ interfaces: magnetism and orbital ordering. *New J. Phys.* **15,** 023022 (2013).

35. Michaeli, K., Potter, A. C. & Lee, P. A. Superconducting and ferromagnetic phases in $SrTiO_3/LaAlO_3$ oxide interface structures: possibility of finite momentum pairing. *Phys. Rev. Lett.* **108,** 117003 (2012).
36. Choudhury, N., Walter, E. J., Kolesnikov, A. I. & Loong, C.-K. Large phonon band gap in $SrTiO_3$ and the vibrational signatures of ferroelectricity in $ATiO_3$ perovskites: First-principles lattice dynamics and inelastic neutron scattering. *Phys. Rev. B* **77,** 134111 (2008).
37. Ambler, E., Colwell, J. H., Hosler, W. R. & Schooley, J. F. Magnetization and critical fields of superconducting $SrTiO_3$. *Phys. Rev.* **148,** 280–286 (1966).
38. van Mechelen, J. L. M. *et al.* Electron-phonon interaction and charge carrier mass enhancement in $SrTiO_3$. *Phys. Rev. Lett.* **100,** 226403 (2008).
39. Verbist, G., Peeters, F. M. & Devreese, J. T. Extended stability region for large bipolarons through interaction with multiple phonon branches. *Ferroelectrics* **130,** 27–34 (1992).
40. Meevasana, W. *et al.* Strong energy-momentum dispersion of phonon-dressed carriers in the lightly doped band insulator $SrTiO_3$. *New J. Phys* **12,** 023004 (2010).
41. Copie, O. *et al.* Towards two-dimensional metallic behavior at $LaAlO_3/SrTiO_3$ Interfaces. *Phys. Rev. Lett.* **102,** 216804 (2009).
42. Caviglia, A. D. *et al.* Two-dimensional quantum oscillations of the conductance at $LaAlO_3/SrTiO_3$ interfaces. *Phys. Rev. Lett.* **105,** 236802 (2010).
43. Kim, M. *et al.* Fermi surface and superconductivity in low-density high-mobility δ-doped $SrTiO_3$. *Phys. Rev. Lett* **107,** 106801 (2011).
44. Blaha, P., Schwarz, K., Madsen, G., Kvasnicka, D. & Luitz, J. Wien2k package. Available at http://www.wien2k.at.
45. Bahramy, M. *et al.* Emergent quantum confinement at topological insulator surfaces. *Nat. Commun.* **3,** 1159 (2012).
46. Zhang, P. *et al.* A precise method for visualizing dispersive features in image plots. *Rev. Sci. Instrum.* **82,** 043712 (2011).

Acknowledgements

This work was supported by the UK EPSRC (EP/I031014/1), the ERC (207901), the SNSF (200021-146995), the Scottish Funding Council, The Thailand Research Fund (RSA5680052), Office of the Higher Education Commission, Suranaree Univerisity of Technology and the Japan Society for the promotion of Science (JSPS), through the 'Funding Program for World-Leading Innovative R&D on Science and Technology (FIRST Program)', initiated by the council for Science and Technology policy (CSTP). P.D.C.K. acknowledges support from the Royal Society through a University Research Fellowship (UF120096). We acknowledge SOLEIL (beamline CASSIOPEE), the ALS (beamline 10.0.1) and SLS (SIS beamline) for provision of synchrotron radiation facilities, and in particular N.C. Plumb, M. Radovic′ and M. Shi (SLS) and P. Le Fèvre, F. Bertran and A. Taleb-Ibrahimi (SOLEIL) for technical assistance. The Advanced Light Source is supported by the Director, Office of Science, Office of Basic Energy Sciences, of the US Department of Energy under Contract No. DE-AC02-05CH11231. We gratefully acknowledge C. Bell. C. Berthod, V. Cooper, A. Fête, H.Y. Hwang, M. Kim, J. Mannhart, D. van der Marel and J.-M. Triscone for useful discussions.

Author contributions

The experimental data was measured by P.D.C.K., S.M.W., A.T., A.d.l.T., T.E., P.B., W.M. and F.B., and analysed by P.D.C.K., S.M.W., A.T. and F.B. P.D.C.K. and M.S.B. performed the electronic structure calculations and A.T. performed the electron–phonon self-energy calculations. S.-K.M. maintained the ARPES endstation at the Advanced Light Source and provided experimental support. P.D.C.K. and F.B. were responsible for overall project planning and direction, and wrote the manuscript with input and discussion from all co-authors.

Additional information

Supplementary Information accompanies this paper at http://www.nature.com/naturecommunications

Competing financial interests: The authors declare no competing financial interests.

Reprints and permission information is available online at http://npg.nature.com/reprintsandpermissions/

How to cite this article: King, P. D. C. *et al.* Quasiparticle dynamics and spin–orbital texture of the $SrTiO_3$ two-dimensional electron gas. *Nat. Commun.* 5:3414 doi: 10.1038/ncomms4414 (2014).